An Analysis of Elastic Rough Contact Models

by

Yang Xu

A thesis submitted to the Graduate Faculty of
Auburn University
in partial fulfillment of the
requirements for the Degree of
Master of Science

Auburn, Alabama
Aug 04, 2012

Keywords: Rough Surfaces Contact, Elastic, Statistical Model, Boundary Element Model,
Finite Element Model

Approved by

Dan Marghitu, Co-Chair, Professor of Mechanical Engineering
Robert Jackson, Co-Chair, Associate Professor of Mechanical Engineering
Hareesh Tippur, McWane Professor of Mechanical Engineering
George Flowers, Dean, Graduate School

Abstract

The problem of elastic contact between one nominally flat rough surface and one rigid flat is studied. A variety of contact models have been applied to this problem since the pioneering work of Archard in 1956. Those contact models can be divided into 4 categories namely, the statistical, multi-scale, semi-numerical and deterministic numerical models. In Chapter 1, the methods of describing and generating rough surfaces are introduced. Additionally, the Hertzian contact theory is briefly illustrated. In Chapter 2, the developments of the statistical, multi-scale and semi-numerical models are reviewed briefly by introducing several important models, e.g., the Greenwood-Williamson (GW) model. The contact area to load relations predicted by those models are compared to that by deterministic numerical model (the finite element model) which is treated as the "exact" solution. In Chapter 3 and 4, the developments and applications of two popular deterministic numerical methods namely, the boundary element method (BEM) and the finite element method (FEM), for the elastic rough surface contact are reviewed in detail. The contact area to load relations predicted by the BEM and the FEM are compared. The contact areas and the contact pressure distributions at different stages of deformation are also explored. Conclusions of this study can be drawn in the following aspects: (1) the asperity-based models, e.g., the statistical and semi-numerical models, are only valid for low load condition, (2) the simplified multi-scale model is good for both early contact and complete contact, (3) the contact area to load relations predicted by the FEM and the BEM have very good agreement, at least for the case of isotropic surfaces.

Table of Contents

List of Figures

List of Tables

B_{max}　　Maximum value of B

d　　　Surface separation between the rigid flat and the mean level of undeformed rough surface

d'　　　Surface separation between the rigid flat and the mean level of deformed rough surface

d^*　　　Dimensionless surface separation, $d^* = d/\sigma$

E^*　　　Effective material modulus, $E^* = [(1 - \nu_1^2)/E_1 + (1 - \nu_2^2)/E_2]^{-1}$

$E_1,\ E_2$　Young's modulus of contact body 1 and 2

g　　　Gap between the rigid flat and the deformed rough surface

G, D　　Fractal parameters

H　　　Thickness of the substrate of the rough surface

h　　　Rough surface height

H'　　　Hurst exponent

$h'_x,\ h''_x$　Slope and curvature in the x direction

$h'_y,\ h''_y$　Slope and curvature in the y direction

$K_{ijkl}(D_{ms})$　Influence function

$L_x,\ L_y$　Sampling length in the x and y directions

m_0, m_2, m_4　Spectral moments

P　　　Total contact load

p　　　Pressure distribution

P^* Dimensionless contact load, $P^* = P/(E^* A_n)$

R Average radius of asperities or effective radius in the Hertzian contact theory, $R = (R_1^{-1} + R_2^{-1})^{-1}$

$R(\tau)$ Autocorrelation function

R_a Center-line average

$R_q(\sigma)$ Root mean square (RMS) roughness

R_x, R_y Radius of asperity in the x and y directions

$S(w)$ Power spectrum density

Sy Yield stress

w Rough surface deformation

Chapter 1

Introduction

1.1 Rough surface geometry

1.1.1 Statistical description of rough surface

In this section, methods of describing rough surface geometries are introduced. Two popular ways of generating the rough surface by computer code will be discussed. At the end of this section, details of two rough surfaces data, one generated by computer code and another obtained from profilometer, will be illustrated. These two rough surface data will be used as the inputs of all the elastic rough surfaces contact models discussed in the rest of the thesis.

Figs. 1.1 and 1.2 illustrate the typical *rough surface* and *rough surface profile* along the x direction at certain y coordinate measured by profilometer. Fig. 1.3 shows a 2D asperity profile from the rough surface profile in Fig. 1.2. The peaks on the rough surface or rough surface profile are called *asperities*. Sampling points, $i-2, i-1, i, i+1$ and $i+2$, and their connecting lines form the profile of a 2D asperity in Fig. 1.3. Sampling point on the asperity is called *summit*, i in Fig. 1.3, when its height is larger than all of its neighboring sampling points, $i-1$ and $i+1$.

If we neglect the surface roughness when two elastic bodies are in contact, the corresponding contact area is called *nominal contact area*, A_n. When the contact interfaces are rough, the *real contact area*, A_r, is a fraction of nominal contact area, A_n. The ratio of A_r to A_n is called the *contact ratio*.

According to the size, rough surface features can be divided into 3 categories [1] namely, *macrodeviation*, *waviness* and *roughness*. Surfaces of road and landscape are belonging to
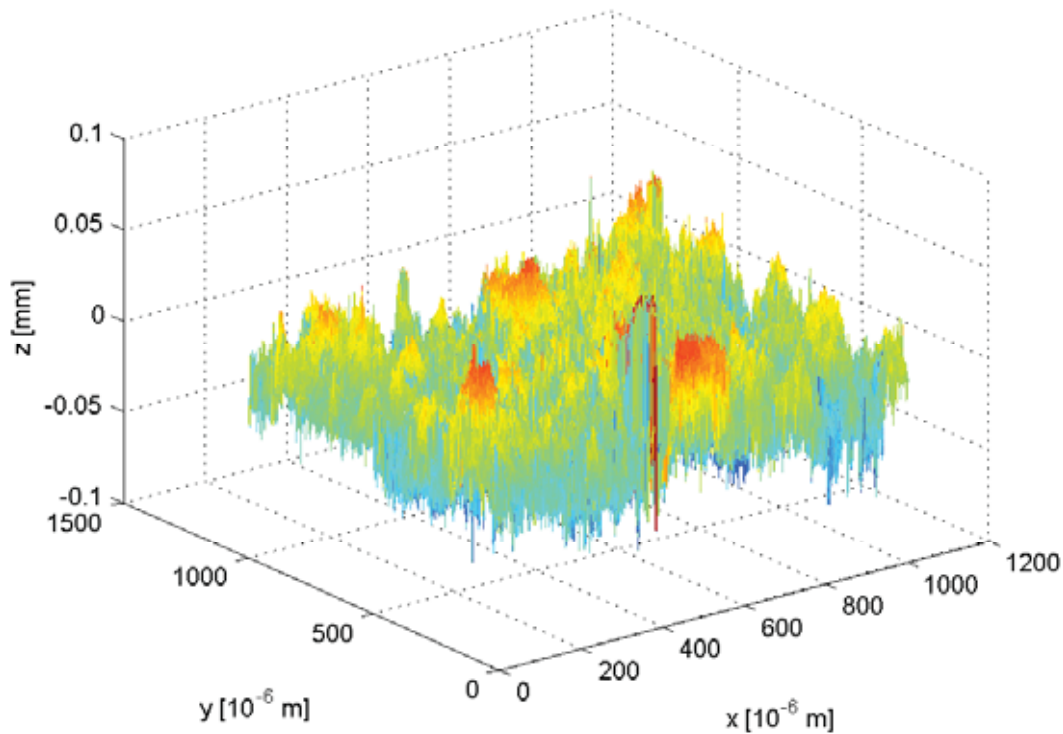
Figure 1.1: Real rough surface measured by profilometer.

macrodeviation because the asperity height of those surfaces is within macroscale and usually the ratio of amplitude to wavelength is considerably large. For waviness surfaces, the ratio of distance between neighboring asperities to the asperity height is usually more than 40 [1]. However, the waviness profile is still visible. Roughness are defined as peaks and valleys which have very small value of height deviations comparing to dimensions of *sampling length* (length of nominal contact area) and are generally invisible to the unassisted eye.

It is difficult to describe rough surface deterministically due to its *multi-scale* structure, which will be discussed later, and random nature. Therefore, simplifying mathematics such as *statistical parameters* are used. Here we only illustrate the statistical parameters of a *rough surface profile* (2D). Extension to *rough surface* (3D) is very similar to the 2D case. $h_i, i = 1, ..., N$ is the height of rough surface profile obtained from a profilometer with the resolution Δ_x and one small portion of a rough surface profile with 15 sampling points is

2
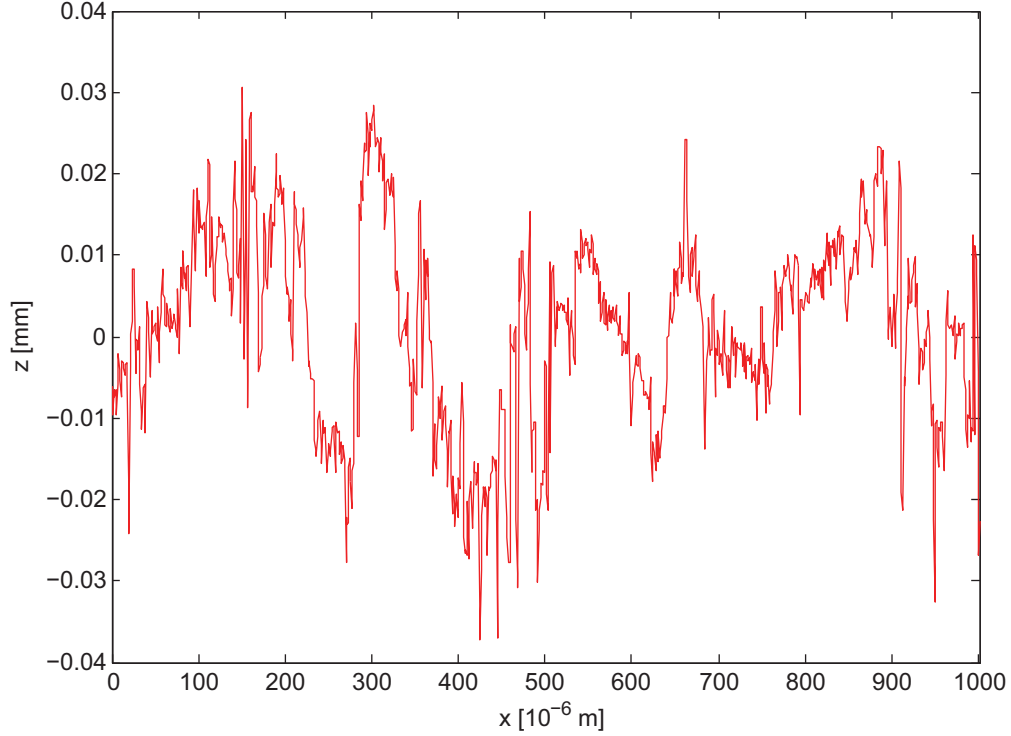
Figure 1.2: Real rough surface profile measured by profilometer.

plotted in Fig. 1.4. N is number of sampling points. R_a, *center-line average*, describes the roughness of rough surface profile

$$R_a = \frac{1}{N} \sum_{i=1}^{N} |h_i|$$

and level at the average height of surface profile is called *mean level*. Another similar parameter, the *root mean square* (*RMS*) roughness, σ or R_q, is also widely used as a measurement of average roughness

$$\sigma = \sqrt{\frac{1}{N} \sum_{i=1}^{N} h_i^2}$$

and σ is more sensitive to large deviations from the mean level [2]. However, the center-line average, R_a, and root mean square, σ, cannot uniquely describe the rough surface profile
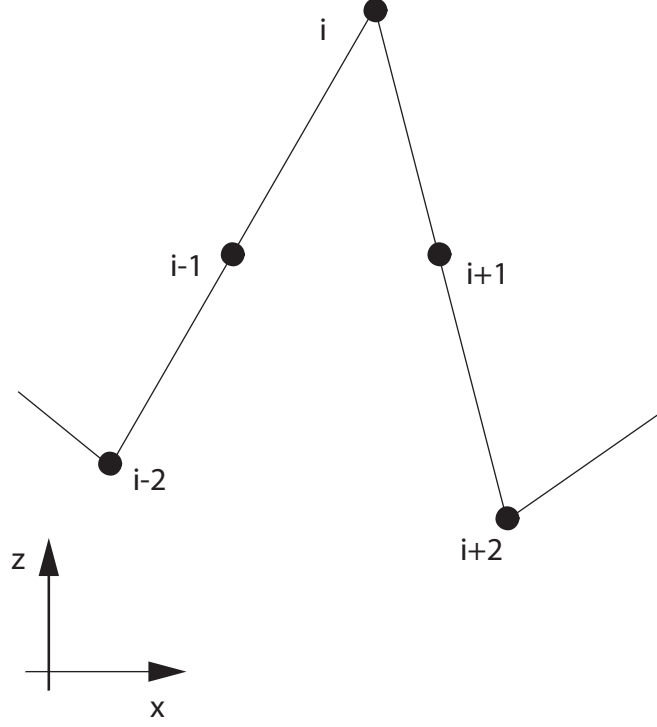
Figure 1.3: Details of a 2D asperity profile in rough surface profile in Fig. 1.2

statistically, thus the spectral moments method are introduced [11]

$$m_0 = \frac{1}{N} \sum_{i=1}^{N} h_i^2$$

$$m_2 = \frac{1}{N-2} \sum_{i=2}^{N-1} h_i'^2$$

$$m_4 = \frac{1}{N-2} \sum_{i=2}^{N-1} h_i''^2.$$

h_i' and h_i'' are the slope and curvature of sampling point i, respectively. h_i' and h_i'' can be numerically determined by using central difference

$$h_i' = \frac{h_{i+1} - h_{i-1}}{2\Delta_x}$$
$$h_i'' = \frac{h_{i+1} - 2h_i + h_{i-1}}{\Delta_x^2}, \quad i = 2, ..., N-1. \tag{1.1}$$
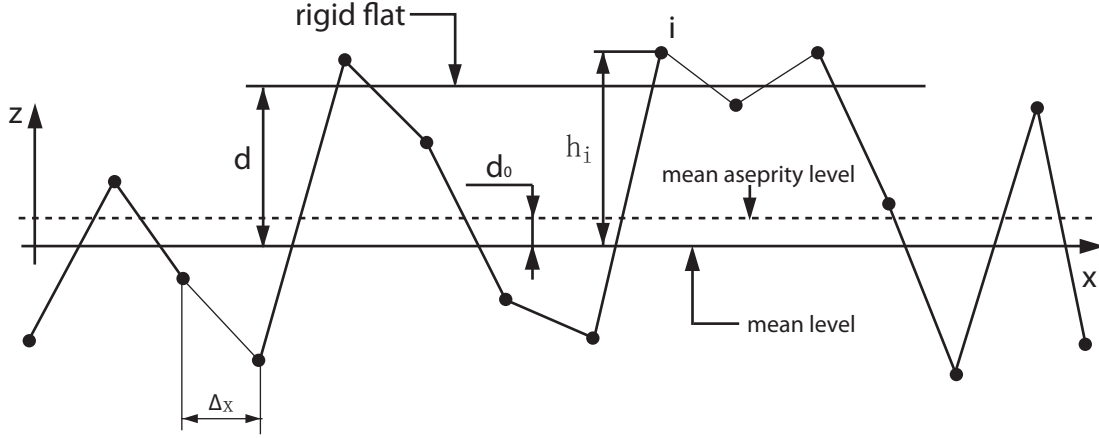
Figure 1.4: Details of a 2D rough surface profile with 15 sampling points from Fig. 1.2

m_0 is the same as the square of σ, i.e., $m_0 = \sigma^2$. m_2 and m_4 are called skewness (SK) and Kurtosis (K) and commonly normalized by σ^2 and σ^4.

In many elastic rough surfaces models, only the heights of the summits are used as the input due to the fact that contacts dominantly occur on asperities. Greenwood and Williamson [3] found that asperity height in many real surfaces can be described by a *Gaussian distribution*

$$\Phi(h) = \frac{1}{\sqrt{2\pi}\sigma_s}\exp\left(\frac{-\text{h}^2}{2\sigma_\text{s}^2}\right)$$

where surface height is centered about the *asperity mean level*, see Fig. 1.4. σ_s is the root mean square of the asperity height (σ is the root mean square of the rough surface profile). Asperity mean level is determined by averaging the asperity heights.

1.1.2 Method of generating rough surface

Commonly, rough surface data is obtained using a profilometer. For model evaluation, an alternative is to generate *fractal surfaces*, which will be discussed later, by the computer code. Two popular algorithms of generating fractal surfaces namely, the *Weierstrass-Mandelbrot* function and the *Random Midpoint Algorithm*, can be found in the past literatures.

Fractal geometry

Fractal geometry [22, 23] can be used to characterize the multi-scale nature of the rough surfaces. A fractal geometry should be *continuous*, *non-differentiable* and *statistically self-affine*, in a mathematical sense. Real rough surfaces obtained from profilometer show exactly the continuous and non-differentiable properties. If a similar surface profile is obtained as the sampling resolution Δ_x decreases, it can be described as statistically self-affine. Due to the above reasons, fractal geometries can be used to approximate real rough surfaces with a multi-scale structure. It is found that the *Weierstrass-Mandelbrot* (WM) function meets all the properties of a fractal geometry. The following WM function [23] can be used

$$h(x) = G^{(D-1)} \sum_{n=n_1}^{n_{max}} \frac{\cos(2\pi\gamma^n x)}{\gamma^{(2-D)n}}, \quad 1 \leq D \leq 2 \tag{1.2}$$

to approximate the real 2D rough surface profile. G is the length scale of the rough surface profile. D is the fractal dimension. γ^n describes the frequency spectrum of the surface roughness. n_1 and n_{max} relate to the cut-off frequencies which are dependent on sampling length L_x and sampling resolution Δ_x. Since a rough surface profile has a finite length, frequency cannot be less than the lowest frequency $\gamma^{n_1} \leq 1/L_x$. Also, the rough surface profile does not have any surface height information beyond the highest frequency level $\gamma^{n_{max}} \geq 1/\Delta_x$. For a 3D rough surface [24, 25], rough surface height can be written as

$$h(x,y) = L \left(\frac{G}{L}\right)^{(D-2)} \left(\frac{ln\gamma}{M}\right)^{1/2} \sum_{m=1}^{M} \sum_{n=1}^{n'_{max}} \gamma^{(D-2)n} \{\cos(\phi_{m,n}) -$$
$$\cos\left[\frac{2\pi\gamma^n(x^2+y^2)^{1/2}}{L}\cos\left(\tan^{-1}\left(\frac{y}{x}\right) - \frac{\pi m}{M}\right) + \phi_{m,n}\right]\}, \quad 2 \leq D \leq 3 \tag{1.3}$$

where $n'_{max} = \text{int}\left(\frac{\log(L/\Delta)}{\log\gamma}\right)$ is the maximum frequency level. L and Δ are the sampling length and sampling resolution (same in the both directions) of the 3D fractal surface, respectively. M denotes the number of superposed ridges used to construct the surface. $\phi_{m,n}$ is a random variable which can be achieved by any random generator. Majumdar and Tien [27] showed $\gamma = 1.5$ is a suitable value for high spectral density and phase randomization.

6

Fractal parameters G and D can be extracted from rough surface data. A fourier transformation of the *autocorrelation function* $R(\tau)$ of fractal surfaces generated by Eq. 1.2 and 1.3, i.e., the *power spectrum density* $S(w)$, may result in the following power law form

$$S(w) = \frac{G^{2(D-1)}}{2ln\gamma} \frac{1}{w^{(5-2D)}} \tag{1.4}$$

where w is the frequency of roughness. If $S(w)$ is plotted in a log-log plot, D is related to the slope of $S(w)$ and G can be extracted from $S(w = 0)$. It is obvious that G and D are scale-independent parameters comparing to the scale-dependent surface parameters, e.g., m_0, m_2 and m_4 [27, 26].

Random Midpoint Algorithm

Another way of generating self-affine fractal surface, which is called *random midpoint algorithm*, is developed by Voss [28]. In stead of scale-invariant fractal parameters used in WM function, Eqs. 1.2 and 1.3, only one parameter H', *Hurst exponent*, is needed. The relationship between Hurst exponent and Fractal dimension is: $H' = 3 - H(3D)$ and $H' = 2 - H(2D)$.

1.1.3 Rough surfaces data used in this study
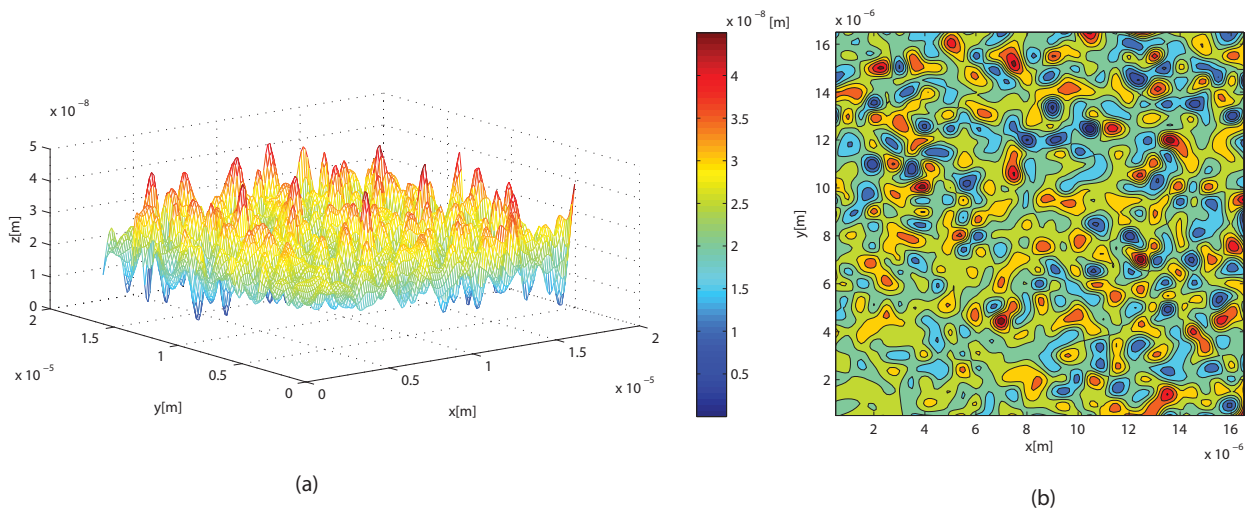
Figure 1.5: 3 dimensional profile (a) and colored contour (b) of surface 1, i.e., fractal surface.

7

Table 1.1: Statistical and fractal parameters of two surfaces

Parameter	Surface 1	Surface 2	Parameter	Surface 1	Surface 2
m_0 (m^2)	6.7081×10^{-16}	5.9061×10^{-14}	m_{2x}	3.6506×10^{-4}	2.6607×10^{-5}
m_{4x} (m^{-2})	8.2388×10^{9}	8.7907×10^{5}	m_{2y}	3.9087×10^{-4}	9.7553×10^{-5}
m_{4y} (m^{-2})	9.1915×10^{9}	2.3517×10^{7}	σ_s(m)	3.4070×10^{-8}	2.4331×10^{-7}
η_s (m^{-2})	8.8281×10^{11}	1.3600×10^{9}	R(m)	1.2098×10^{-5}	0.0013
G (m)	9.4600×10^{-14}		D	2.4400	
L_x (m)	1.6000×10^{-5}	9.9200×10^{-4}	L_y (m)	1.6000×10^{-5}	9.9200×10^{-4}
Δ_x (m)	1.25×10^{-7}	8×10^{-6}	Δ_y (m)	1.25×10^{-7}	8×10^{-6}

(a)

(b)
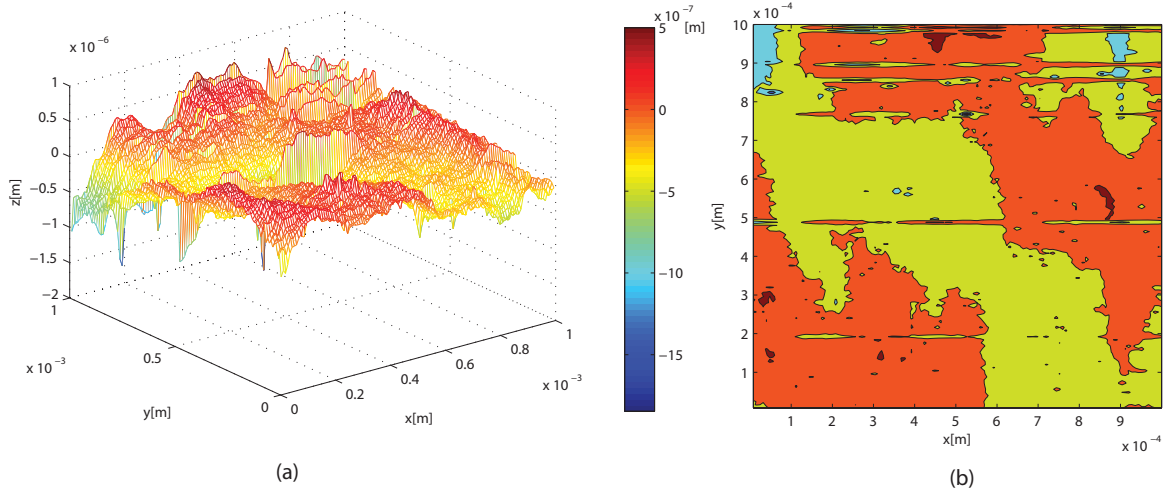
Figure 1.6: 3 dimensional profile (a) and colored contour (b) of surface 2, i.e., real rough surface.

Two rough surfaces data namely, surface 1 and surface 2, are used throughout the rest of the thesis as the inputs of all the elastic rough surfaces contact model. Surface 1 is generated by the WM function, Eq. 1.3, and surface 2 is measured by profilometer from a standard rough surface sample. The main statistical and fractal parameters are illustrated in Table. 1.1. η_s and R are the asperity density and average radius of asperity, respectively. η_s is the ratio of number of asperities to the nominal area A_n. The radius of curvature, R_i, of each

asperity i can be defined as

$$R_i = (R_x + R_y)/2 \tag{1.5}$$

$$R_x = (1 - (h'_x)^2)^{1.5}/h''_x$$

$$R_y = (1 - (h'_y)^2)^{1.5}/h''_y,$$

h'_x, h'_y, h''_x and h''_y are slopes and curvatures of asperity i along x and y directions (Eq. 1.1). L_x and L_y are sampling lengths in x and y directions, $A_n = L_x \times L_y$. Δ_x and Δ_y are the resolutions along x and y directions. Surface 1 consists of 129×129 sampling points and surface 2 is 125×125.

m_2 and m_4 along both x and y are m_{2x}, m_{2y}, m_{4x} and m_{4y} and are listed in Table 1.1. Differences between spectral moments of surface 1 in the x and y directions are negligible comparing to that of surface 2. However, they differ greatly for surface 2. Consequently, surface 1 can be treated as an isotropic surface and surface 2 as an anisotropic surface.

1.2 Single asperity contact

Between two approaching rough surfaces, contacts initially occur at the *summits* of asperities. Thus, at low load conditions, the majority of contact areas grow independently (without interactions between them). Thus the resultant rough surface contact load P and contact area A are the superpositions of contact load $\bar{P}$, and the area of single contacting asperities $\bar{A}$.

$$P = \sum_{i=1}^{N_c} \bar{P}_i$$

$$A = \sum_{i=1}^{N_c} \bar{A}_i \tag{1.6}$$

Note that N_c is the number of contacting asperities at a given surface separation d. Commonly, rough surface contact models are called *asperity-based contact models* if Eq. 1.6 is

used to obtain the total contact force P and area A. As a result, it is necessary to derive an accurate *single asperity contact model* for the elastic contact accounting for different shapes of contact interfaces.

It is unlikely to accurately approximate the complex shapes of asperities using simple geometrical entities. At the low load condition, nearly all the contacts occur near the tips of the asperities and many efforts have been put on modeling the geometry of the tip of asperity and its corresponding asperity contact model. The most popular geometrical entity used to approximate the shape of tip is a *hemisphere*, see Fig. 1.7.

1.2.1 Elastic asperity contact
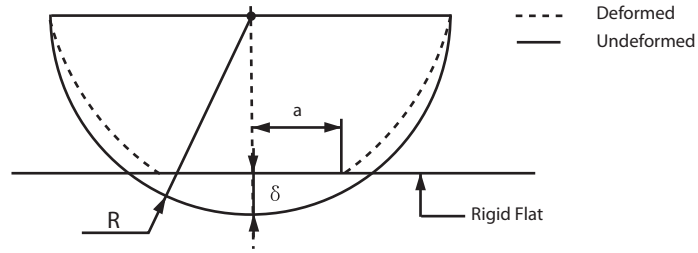
Figure 1.7: Asperity contact model

As we mentioned before that spherical cap is the most popular geometrical entity to approximate the tip of asperities where contacts are more likely to occur, thus the well-known *Hertzian spherical contact theory* can be used here to model the contact between two hemispherical caps of radius R_1 and R_2, respectively. Contact between two hemispherical caps can be further simplified to the contact between an equivalent hemispherical cap and one rigid flat, see Fig. 1.7. The *effective radius*, R, can be written as

$$R = (R_1^{-1} + R_2^{-1})^{-1}$$

and the Young's modulus of the equivalent hemispherical cap (*effective material modulus*, E^*) is

$$E^* = [(1 - \nu_1^2)/E_1 + (1 - \nu_2^2)/E_2]^{-1}$$

10

where E_i and ν_i, $i = 1, 2$, are Young's modulus and Poisson's ratio of the two hemispherical caps, respectively. In the rest of the article, the contact between two asperities will always be simplified as the contact between one asperity of effective radius R and one rigid flat. Thus the contact area, $\bar{A}$, and contact load, $\bar{P}$, due to contact between two hemispherical caps, are described by Hertz [32]

$$\bar{A} = \pi a^2 = \pi R \delta \tag{1.7}$$

$$\bar{P} = \frac{4}{3} E^* R^{\frac{1}{2}} \delta^{\frac{3}{2}}. \tag{1.8}$$

where a is the radius of contact area. δ is the deflection (or penetration, indentation) as illustrated in Fig. 1.7. The pressure distribution defined in polar coordinate, $p(r)$, within the contact area is

$$p(r) = p_0 \sqrt{1 - r^2/a^2}, \quad r \in [0, a]$$

where p_0 is maximum contact pressure.

Commonly, critical deformation, δ_c, is used to predict the onset of yielding in the sphere. Yielding first occurs beneath or on the contact interface between two asperities with hemispherical tips. When deformation is larger than δ_c, i.e., $\delta > \delta_c$, deformation beneath or on the contact interface may become elastoplastic. For the ductile material, the onset of first yield is governed by the *von-Mises criterion*. Chang et al [4] and Jackson and Green [5] derived similar expressions of δ_c based on the von-Mises criterion. The one from Jackson and Green is

$$\delta_c = \left(\frac{\pi p_0}{2E^*} \right)^2 R$$

where

$$p_0/S_y = 1.295 \exp(0.736\nu)$$

where S_y is the yield stress of the material in unidirectional tension (or compression). S_y and ν are the values corresponding to the minimum p_0. For the brittle materials, onset of

first yield is governed by *Tresca maximum tensile stress criterion* and the corresponding δ_c is derived numerically by Brizmer et al[6].

The above derivation of critical deformation δ_c is only valid for the perfect slip condition. δ_c for full stick conditions can be found in [6]. δ_c for the partial slip condition is currently not available.

Chapter 2

Statistical, multi-scale and semi-numerical rough surfaces contact model

2.1 Statistical rough surfaces contact model

The statistical type of contact model is still the most popular model used in rough surfaces contact. In stead of using the complete roughness data, only *probability density function* $\Phi(h)$ is used. $\Phi(h)$ means the probability of the asperity with the height between h and $h + dh$. Assume we know the exact expression of $\Phi(h)$, then the number of asperities with height h is

$$N(h) = \Phi(h)\bar{N}$$

where $\bar{N}$ is the total number of asperities in the rough surface. Thus, the total contact load (P) and area (A) as a function of d can be written as

$$P(d) = \bar{N} \int_{d}^{+\infty} \bar{P}\Phi(h)\,dh \tag{2.1}$$

$$A(d) = \bar{N} \int_{d}^{+\infty} \bar{A}\Phi(h)\,dh \tag{2.2}$$

d is the surface separation between rigid flat and mean asperity level, see Fig. 1.4. Deformation δ of each contacting asperity is

$$\delta = h - d$$

Commonly, two rough surfaces contact can be simplified as one equivalent rough surface contacting a rigid flat. The height of equivalent surface, $h(x)$, can be written as $h(x) =$

$h_1(x) + h_2(x)$. h_1 and h_2 are two rough surfaces. Additionally, the spectral moments, m_0, m_2 and m_4, of the equivalent rough surface profile are

$$m_0 = (m_0)_1 + (m_0)_2 \tag{2.3}$$

$$m_2 = (m_2)_1 + (m_2)_2 \tag{2.4}$$

$$m_4 = (m_4)_1 + (m_4)_2 \tag{2.5}$$

$(m_0)_i, (m_2)_i$ and $(m_4)_i, i = 1, 2$, are spectral moments of two rough surfaces. Eq. 2.1 was first developed by Greenwood and Williamson [3].

2.1.1   Greenwood-Williamson (GW) model

In 1966, Greenwood and Williamson combined random process with classical Hertzian contact to deal with rough surfaces contact. In their pioneering theory, they adopted the following assumptions:

1. The asperity height distribution is Gaussian, i.e., the probability density function $\Phi(h)$ is

$$\Phi(h) = \frac{1}{\sqrt{2\pi}\sigma_s} \exp\left(-\frac{h^2}{2\sigma_s^2}\right) \tag{2.6}$$

where σ_s is the standard deviation of asperity height. The asperity height h is centered about *mean asperity level*.

2. Asperity contact is modeled by the Hertzian spherical contact theory (Eq.1.7);

3. The radius of all asperities are assumed constant (R);

4. Ignore adhesion, shoulder-shoulder contact, neighboring asperity interaction and asperity coalescing.

By using dimensionless asperity height $h^* = h/\sigma_s$ and dimensionless surface separation $d^* = d/\sigma_s$. Asperity probability density function $\Phi(h^*)$, total contact load $P(d^*)$ and area

$A(d^*)$ in the GW model can be written as

$$\Phi(h^*) = \frac{1}{\sqrt{2\pi}}\exp\left(-\frac{(h^*)^2}{2}\right) \tag{2.7}$$

$$P(d^*) = A_n \eta_s \int_{d^*}^{+\infty} \bar{P}\Phi(h^*)\,dh^* \tag{2.8}$$

$$A(d^*) = A_n \eta_s \int_{d^*}^{+\infty} \bar{A}\Phi(h^*)\,dh^* \tag{2.9}$$

A_n and η_s are nominal contact area and asperity density, respectively. Multiplication of A_n and η is the total number of asperities in the rough surface sample ($\bar{N}$). $\bar{P}$ and $\bar{A}$ are calculated by Eq. 1.7.

2.1.2 Advanced statistical models

Whitehouse and Archard (WA) model

Whitehouse and Archard [9] (WA) abandoned the assumption of a constant asperity radius. Rough surfaces obtained from a profilometer show that higher asperities have sharper tips. Whitehouse and Archard incorporated this correlation into the surface statistics and assumed an exponential-like autocorrelation function, $R(\tau)$. They derived the joint probability density function, $\Phi(h^*, C)$, of both summit height and summit curvature. C is a non-dimensional summit curvature. Their joint probability density function was used by Onions and Archard [10] in deriving elastic contact load (P) and area (A) following the framework of the GW model, Eq. 2.7.

Nayak Model

Nayak [11] (1971) derived more generalized joint probability functions for both surface profile (2D) and rough surfaces (3D) based on 2 and 3 dimensional joint probability function: $\Phi(h, \frac{\partial h}{\partial x}, \frac{\partial^2 h}{\partial x^2})$ and $\Phi(h, \frac{\partial h}{\partial x}, \frac{\partial h}{\partial y}, \frac{\partial^2 h}{\partial x^2}, \frac{\partial^2 h}{\partial x \partial y}, \frac{\partial^2 h}{\partial y^2})$.

Bush et al (BGT) Model

For simplicity, the curvatures of the contacting summits used in Nayak's statistical model is mean curvature $\kappa_m = (-\frac{\partial^2 h}{\partial x^2} + \frac{\partial^2 h}{\partial y^2})/2$ and Hertzian spherical contact theory is used. Bush et al [12] (BGT) (1975) extended the Nayak statistical model by considering two principle curvatures of asperities along the x and y directions. Asperity contact model in the BGT model becomes more generalized Hertzian elliptic contact model. Due to its complexity, only the asymptotic solution of the BGT model [14] is written here

$$A/A_n = \sqrt{\frac{\pi}{m_2}} \frac{P}{E^* A_n} \tag{2.10}$$

which has a linear relation between contact area A and contact load P.

McCool Model

The above mentioned advanced statistical models all introduced more than one random variables in their joint probability density function Φ which cause their models to be more complex (multiple integrals) than the GW model and inconvenient to apply. The GW model has a clean-cut expression but the inaccurate inputs of asperity density η_s, asperity r.m.s σ_s and constant radius R may cause the inaccurate contact load (P) and area (A). McCool [13] (1987) derived the following closed-form expression of inputs for GW model

$$\eta_s = \frac{1}{6\pi\sqrt{3}} \left(\frac{m_4}{m_2} \right) \tag{2.11}$$

$$R = 0.375 \left(\frac{\pi}{m_4} \right)^{0.5} \tag{2.12}$$

$$\sigma_s = \left(1 - \frac{0.8968}{\alpha} \right)^{0.5} m_0^{0.5} \tag{2.13}$$

based on the Nayak statistical model for isotropic rough surfaces. $\alpha = \frac{m_0 m_4}{m_2^2}$ is called the *bandwidth parameter* introduced by Nayak [11].

Zhao and Chang (ZC) Model and Ciavarella et al (CGP) Model

In the above statistical models, the substrate beneath the rough surface is assumed to be rigid, thus the interaction between the neighboring asperities due to the elastic deformation

16

of substrate is neglected and the local asperity deformation is calculated as: $\delta = h - d$. Due to the asperity interaction, the contact load may cause the redistribution of asperity height. Consequently, the probability density function Φ of undeformed asperity distribution may no longer be the same. Zhao and Chang (ZC)[15] derived a modified asperity deformation equation

$$\delta = h - d + 1.12\frac{\sqrt{w_l p_m}}{E^*}$$

by introducing the displacement of the mean asperity level caused by contact load. w_l is the contact load on the single asperity and p_m is the average pressure over the nominal contact area A_n, i.e., $p_m = P/A_n$. When modified asperity deformation δ is applied in the GW model, Eq. 2.7, the modified GW model becomes nonlinear and the iterative method has to be used in order to obtained a convergent solution. Ciavarella et al (CGP) [16] derived a similar modified asperity deformation equation.

$$\delta = h - d - p_m A_n^{1/2}/E^*$$

A comprehensive comparison between GW+McCool (GW model with McCool's inputs), full BGT and Nayak models have recently been performed by Carbone and Bottiglione [14]. Two important conclusions have been drawn:

1. The contact area-load curve of all the models quickly deviate from the linear relation obtained at the light load condition.

2. The slope of contact area-load curve predicted by BGT and Nayak models converges to unity as surface separation d reaches a very high value with vanishing contact load and area. However, GW+McCool doesn't have such unity slope at high values of d.

Even though the advanced statistical models, e.g., Nayak and BGT models, are derived from a complete joint probability density function with multiple random variables, they are proved to be inaccurate by numerical simulations [34] at medium and heavy load conditions. The major reason that causes the inaccuracy is that the statistical model is based on single

asperity contact model. At the low load condition (small contact area and large surface separation), the majority of contact areas of single asperities grow independently, i.e. no asperity coalescing occurs. Thus the contact load and area are the summation of contact loads and areas on single asperities. The contact load-area curve shows a linear relation only at vanishing load condition. When rough surface contact reaches medium and even heavy load conditions, asperity coalescing becomes more and more severe. Usually statistical models may therefore overestimate both the contact area and load [34].

2.2 Multi-scale model

Experimental results [2, 23, 26] show that the statistical surface parameters, e.g., spectral moments m_0, m_2 and m_4, are dependent on *sampling resolution*. Consequently, results of statistical model may deviate from each other if the same rough surface is measured with different resolutions. Due to the multi-scale nature of rough surfaces, Archard [21] developed the first multi-scale elastic rough surfaces contact model (perhaps the first rough surface contact model). The structure of rough surfaces used in Archard's model is described as "protuberances on protuberances" type. Each protuberance has the hemispherical shape and more smaller protuberances are uniformly distributing on its surface. As more scales are being involved, the contact area-load relation approaches linearity. However, Archard's multi-scale model cannot be practically used on a real rough surface because of its unrealistic rough surface structure.

2.2.1 Majumdar and Bhushan (MB) fractal contact model

Majumdar and Bhushan (MB)[23] developed the first elastic multi-scale contact model based on fractal geometry. The MB model can only deal with a 2-D rough surface profile with the fractal dimension D lying between 1 and 2. They assumed that the contact spot distribution $n(a)$ is

$$n(a) = \frac{D}{2} \frac{a_l^{D/2}}{a^{D/2+1}} \tag{2.14}$$

where a_l is the maximum contact spot area and can be calculated by $a_l = A\frac{2-D}{D}$. A is the contact area and can be obtained by the relation

$$A/A_n = \frac{1}{\sqrt{2\pi}\sigma} \int\limits_{d}^{+\infty} exp(-h^2/2)\, dh \tag{2.15}$$

which assumes that the surface profile follows a Gaussian distribution. σ is the r.m.s of rough surface profile. Actually, the fractal surface can be treated as the stack of sinusoidal waves with random phases based on the mathematical expression (Eq. 1.2), and contact load P calculated in the MB model is the superposition of contact load $\bar{P}$ of different frequency domain. $\bar{P}$ is calculated based on Hertzian spherical contact theory and asperity deformation is assumed as the amplitude of each sinusoidal wave. Then we have

$$P = \int\limits_{0}^{a_l} \frac{4\sqrt{\pi}E^*G^{D-1}a^{(3-D)/2}}{3}n(a)\, da. \tag{2.16}$$

Eq. 2.15 and Eq. 2.16 show a nonlinear relation between A and P. The MB fractal model has been criticized due to the following reasons:

(1) The contact spot distribution, Eq. 2.14, is only geometrically-dependent and it has nothing to do with the elastic properties and contact condition;

(2) The real contact area function, Eq. 2.15, is only valid for the surface follows Gaussian distribution, which is unrealistic for the fractal surface.

(3) Using amplitude of each sinusoidal wave as the asperity deformation is too simplified.

2.2.2 Jackson and Streator (JS) multi-scale model

Jackson and Streator (JS)[29] developed an isotropic 3-D multi-scale contact model based on 3D sinusoidal contact model ([30, 31]). The main ideal of the JS model is that a 2-D rough surface profile can be decomposed into stacks of sinusoidal waves with different frequencies f_i (or wavelength λ_i) and amplitude Δ_i. Asperity density η_i and asperity contact

radius R_i of each sinusoidal waves can be easily determined:

$$\eta_i = 2f_i$$

$$R_i = \frac{1}{4\pi^2 \Delta_i f_i^2}$$

on each frequency level. Johnson et al [31] provided two asymptotic solutions about contact between a sinusoidal surface and a rigid base. When $\bar{p} \ll p^*$,

$$(\bar{A}_{JGH})_1 = \frac{\pi}{f_i^2} \frac{3}{8\pi} \frac{\bar{p}}{p^*}$$

and $\bar{p}$ approaches p^*

$$(\bar{A}_{JGH})_2 = \frac{1}{2f_i^2}(1 - \frac{3}{2\pi}[1 - \bar{p}/p^*])$$

where $\bar{p}$ is the average contact pressure over nominal contact area (λ_i^2) and p^* is the average pressure to cause complete contact

$$p^* = \sqrt{2}\pi E^* \Delta_i / \lambda_i.$$

Jackson and Streator curve-fitted the two asymptotic solutions to bridge the gap between them:

$$\bar{A}_i = (\bar{A}_{JGH})_1 \left(1 - \left(\frac{\bar{p}}{p^*}\right)^{1.51}\right) + (\bar{A}_{JGH})_2 \left(\frac{\bar{p}}{p^*}\right)^{1.04} \tag{2.17}$$

$$\bar{A}_i = (\bar{A}_{JGH})_2 \tag{2.18}$$

The above empirical functions have been validated by both finite element method [33] and FFT-based deterministic model [34]. The assumptions made in the JS model are:

1. Higher frequency domains are superimposed upon lower frequency domain, which is similar to Archard's model [21]. The difference is that the shape of protuberance used in

Archard's model is spherical and while it is sinusoidal in the JS model.

2. Each scale carries the same total load

3. A given scale cannot increase the contact area beyond what is experienced by the frequency level below it. Assumption 3 ensures real contact area, A_r, is bounded ($A_r \leq A_n$) and guarantees the convergence of A_r as frequency level increases.

4. The load at each frequency level is shared equally among all the asperities at that level.

Thus the following contact model can be gained

$$A = \left(\prod_{i=1}^{i_{max}} \bar{A}_i \eta_i \right) A_n \qquad (2.19)$$

$$P = \bar{P}_i \eta_i A_{i-1} \qquad (2.20)$$

By using fast Fourier transformation (FFT), we can decompose the rough surface into i_{max} frequency levels. For a given contact load P, contact load $\bar{P}_i = \bar{p}_i(\lambda_i^2)$ on each asperity within frequency domain i can be determined by Eq. 2.20. Then corresponding contact area $\bar{A}_i$ can be calculated. These steps are iteratively performed until frequency level (i_{max}) is reached. Based on Eq. 2.19, the real contact area (A) can be determined.

Jackson [35] further simplified the JS model by using

$$A = \frac{P}{\sqrt{2\pi} E' B_{max}}, \quad B_{max} = max(B) \qquad (2.21)$$

and this *simplified multi-scale model*, Eq. 2.21, can be applied for both 2D and 3D rough surface data. *For 3D rough surface data, $B = \beta_i/\lambda_i$ is derived by taking the FFT of each 2D row of 3D surface and then averaging the results* [34].

2.3   Semi-numerical deterministic model

In the above sections, we briefly introduced the statistical models, e.g., the GW model, and multi-scale models, e.g., the MB and JS models. In the statistical models, the concept

of *asperity contact* is essential in determining the contact load and area. Additionally, only limited information of roughness, e.g., spectral moments (m_0, m_2, and m_4) in the GW model, is utilized. This is also true for the multi-scale. Only frequencies and amplitudes of each sinusoidal components are used as the inputs. In the next chapter, the application of deterministic numerical methods for rough surface contact will be introduced in detail. Since a majority of contacts occur at the vicinity of asperities, coordinates of asperities (strictly speaking the summits) are essential in predicting the contact load-area relation. This ideal can be achieved by using the coordinates of summits and corresponding radius of curvatures as the inputs. Because the real surface roughness data is still partially utilized, we call the rough surfaces contact models, which adopt the above ideal, the semi-numerical models in this thesis.

Considerable efforts are been placed on the development of semi-numerical deterministic models in the following aspects:

(1) The Radius of curvature distribution are considered and more complex methods of evaluating the radius of curvature at each contact asperity are developed [72, 73, 74];

(2) More accurate asperity interaction models are included [75, 76, 65, 77];

(3) Asperity coalescing is included [78, 79, 80, 81, 77].

The concept of asperity contact is retained which makes these models different from numerical deterministic models. However, in order to model more accurate asperity interaction, asperity coalescing and asperity radius of curvature, coordinates of summits are utilized instead of statistical parameters.

In this section, only one typical semi-numerical deterministic model, developed by Ciavarella et al [75],are introduced.

2.3.1   Ciavarella et al's model

Contact model studied by Ciaverella et al. [75] consists of one rigid rough surface and one elastic half-space. Since only asperities are essential for the rough surface contact

according to the GW model, the rough surface is characterized by the vectors of asperity coordinates **x**, **y** and **z** and radius of curvature **R**. Asperities are determined based on the criterion that it should be the maxima comparing to the neighboring 4 sampling points. The radius of curvature R can be determined by

$$R_x = \frac{(1 - h_x'^2)^{1.5}}{h_x''}$$

$$R_y = \frac{(1 - h_y'^2)^{1.5}}{h_y''}$$

$$R = (R_x + R_y)/2,$$

where h_i' and h_i'', $i = x$ and y, are calculated by Eq. 1.1.

As the rigid rough surface approaches the elastic half-space, the contact areas grow independently on the top surface of the elastic half-space. The shape of each contact area can be determined by Hertzian spherical contact theory:

$$p(r) = p_0 \sqrt{1 - r^2/a^2} \quad r \in [0, a]$$

$$\delta = a^2/R$$

$$a = \left(\frac{3}{4}\frac{\bar{P}\,R}{E^*}\right)^{1/3}. \tag{2.22}$$

p_0 is maximum contact pressure. a is contact area radius. δ is the deformation of asperity. $\bar{P}$ is external load acting on asperity. For a typical Hertzian pressure distribution within the contact area a_j, the corresponding vertical displacement of asperity i, w_i, may be written as [31]

$$w_i = \frac{1}{R_j}(a_j^2 - r^2/2), \quad r \leq a_j \tag{2.23}$$

$$w_i = \frac{1}{\pi R_j}\left[(2a_j^2 - r^2)\mathrm{asin}\left(\frac{a_j}{r}\right) + a_j\sqrt{r^2 - a_j^2}\right], \quad r > a_j \tag{2.24}$$

where r is the distance between asperity i and asperity j: $r = \sqrt{(x_i - x_j)^2 + (y_i - y_j)^2}$. Total displacement of asperity i due to all the Hertzian contact is

$$w_i = \sum_{j=1, i \neq j}^{N_c} \left(\frac{1}{\pi R_j} \left[(2a_j^2 - r^2)\text{asin}\left(\frac{a_j}{r}\right) + a_j\sqrt{r^2 - a_j^2} \right] \right) + \frac{1}{R_i}a_i^2 \qquad (2.25)$$

where N_c is the number of contacting asperities. Eq. 2.25 assumes that only one asperity, itself, lies within the contact area of radius a_i. This assumption is reasonable when contact areas grow independently. However, the prediction of contact load and area at high load conditions may not be accurate due to the fact of *asperity coalescing*. For those contacting asperities, the following governing equation should be obeyed:

$$h_i = d + w_i, \quad i = 1, ..., N_c$$

where h_i is asperity height measured from the mean level. d is surface separation.

Because the contacting asperities are unknown in advance, an iterative scheme needs to be adopted. Ciavarella et al. [75] introduced the following correction scheme

$$\Delta a_i = \frac{R_i}{2a_i}(h_i - d)$$

$$a_{i+1} = a_i + \Delta a_i \qquad (2.26)$$

by differentiating Eq. 2.22. The contact area a_i are updated iteratively until Δa_i is sufficiently small.

2.4 Results and discussion

In the above sections, we have briefly introduced some important models in the development of statistical (GW, Nayak, BGT, ZC and CGP) and multi-scale (Archard, MB and JS) models. In this section, statistical (GW, Nayak, asymptotic BGT and CGP) and

the simplified multi-scale, Eq. 2.21, models are compared to the finite element model, the solution of which is treated as "exact" and will be discussed later.

Surface 1 and surface 2, discussed in the Section 1.1.2, are used as the inputs of the elastic rough surfaces contact models. Surfaces are compressed by the rigid flat. The essential statistical parameters of both rough surfaces needed as inputs for all of the statistical models, are listed in Table 1.1. m_0, m_2 and m_4 are the average values of that along the x and y directions. Contact load (P) contact area (A) are in the dimensionless forms: $P^* = P/(A_n E^*)$, $A^* = A/A_n$.
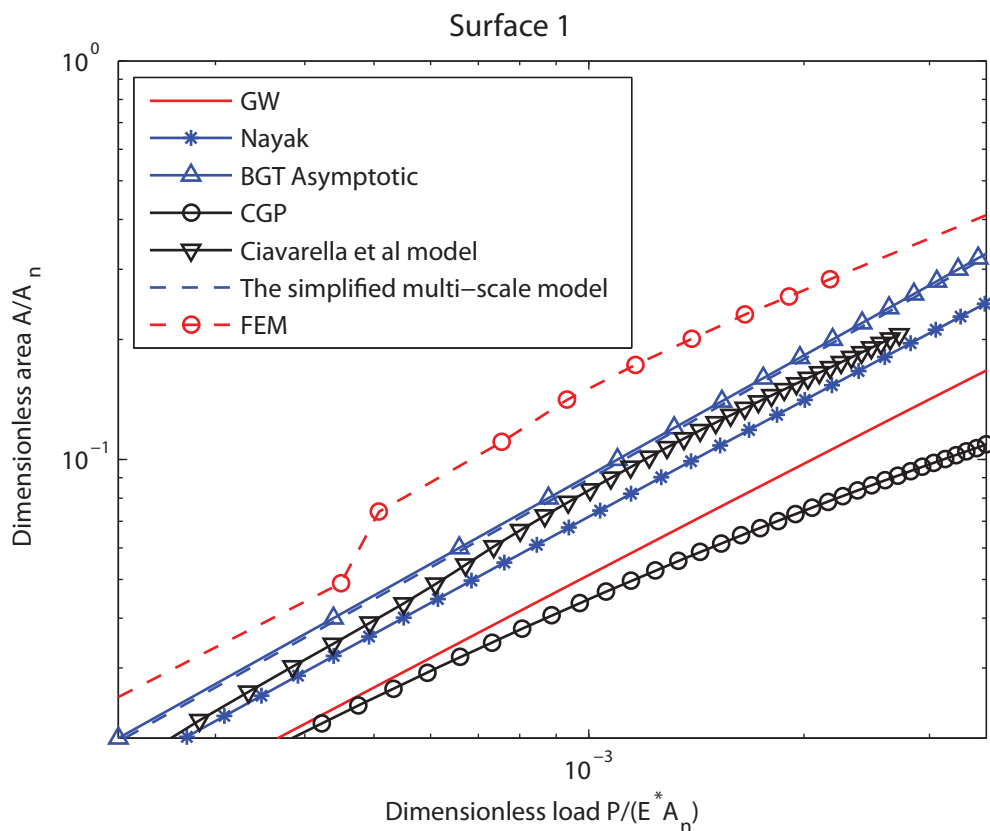
Figure 2.1: Contact area-load relation of surface 1 predicted by statistical, multi-scale and FEM models.

Figs. 2.1 and 2.2 illustrate the relations between A^* and P^* predicted by the GW, Nayak, asymptotic BGT, CGP, Ciavarella et al's semi-numerical model, the simplified multi-scale model and the FE model. Value of B_{max} used in the simplified multi-scale model is the average value of B_{max} of each row of rough surface data.

25
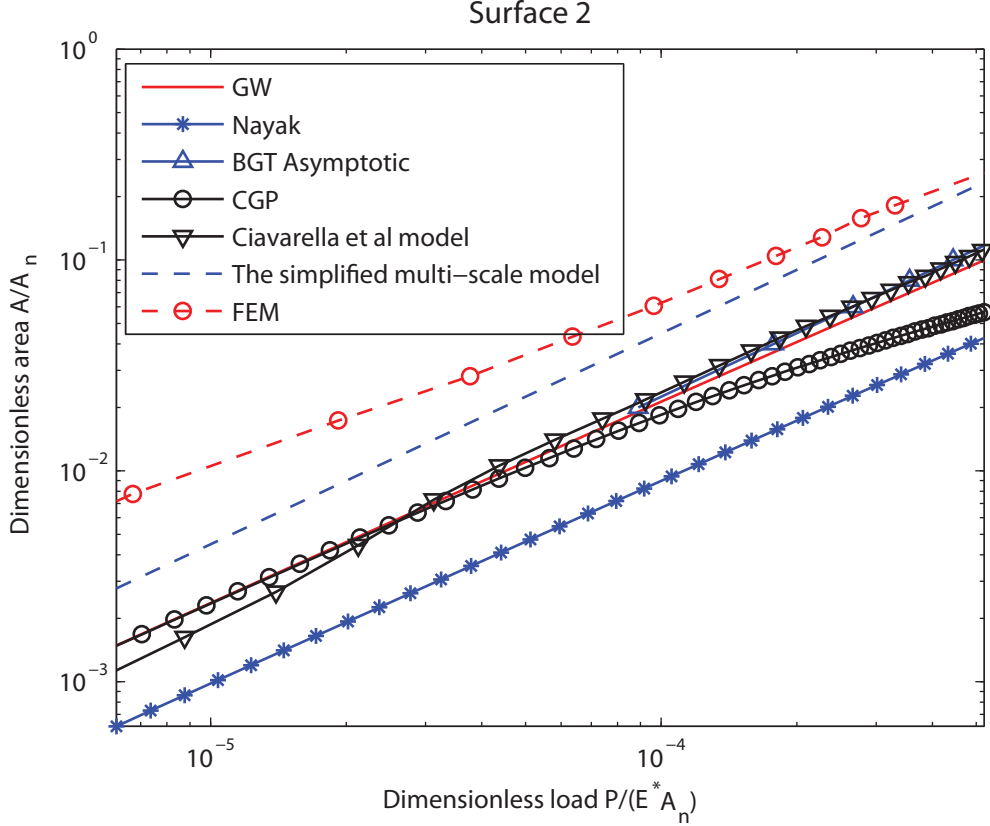
Figure 2.2: Contact area-load relation of surface 2 predicted by statistical, multi-scale and FEM models.

Fig. 2.1 shows the relations between A^* and P^* of (nearly) isotropic surface, e.g., surface 1. All the statistical models discussed above are based on the assumption that the rough surface is isotropic. The asymptotic BGT model has a better accuracy than the GW and Nayak models since it includes both the joint probability function and more generalized elliptic contact model. The multi-scale model is very similar to the asymptotic BGT model. As a results, the Nayak model has a better accuracy than the GW model. At the low load condition, the CGP and GW models have the same prediction because the effect of asperity interaction is not severe. As the load P^* increases, the contact area A^* predicted by the CGP models deviates from that predicted by the GW model. In CGP model, however, only displacement of mean asperity level is used to show the redistribution of asperity height caused by asperity interaction. Relative changes of asperity heights between neighboring asperities are not included. Under the frame work of the statistical models, it is impossible to

include a more accurate asperity interaction model because asperity coordinates are unknown and that is one of the main reasons to develop the semi-numerical deterministic models. Even though Ciavarella et al's semi-numerical deterministic model includes more accurate asperity interaction, its accuracy is only better than that of the Nayak models and worse than that of the BGT model, the simplified multi-scale model and the FE model. Two reasons can explain the defects of Ciavarella et al's semi-numerical deterministic model: (1) Surface 1 is not perfectly isotropic. The spherical asperity contact model used in Ciavarella et al's semi-numerical model may not accurately describe the asperity contact than the more generalized elliptic asperity contact model used in the asymptotic BGT model. (2) Asperity coalescing is not included. It is surprising to see that both the simplified multi-scale and the asymptotic BGT models has the the same and most accurate prediction of the relation between A^* and P^*. This confirms that Archard's type of structure of rough surface combined with sinusoidal protuberances is reasonable to be used in predicting the A^* to P^* relation, although the selection of B_{max} may be important.

Fig. 2.2 illustrates the relations between A^* and P^* of the anisotropic surface, i.e., surface 2. Spectral moments, m_{4x} and m_{4y}, are not in the same order of magnitude, see Table. 1.1, which causes surface 2 to show a strong anisotropic nature. As the results of all the statistical models based upon the isotropic assumption, they may not have good predictions. Ciavarella et al's semi-numerical model uses the spherical asperity contact model and cannot accurately capture the asperity contacts of the anisotropic rough surface (a majority of them are elliptic contacts). The gap between the predictions of the simplified multi-scale and FE models becomes smaller as the load P^* increases within the small load range. The reason of the high accuracy of the simplified multi-scale model is because the parameter B_{max} is the average value of the B_{max} of each row of the rough surface data. This average process may more or less capture the strong effect of anisotropic nature on the relation between A^* and P^*.

Figure 2.3: Contact area-load relation of surface 1 predicted by simplified multi-scale models [34] with different definition of B_{max}.

Figs. 2.3 and 2.4 illustrate the relations between A^* and P^* predicted by the simplified multi-scale and FEM models. Different definitions of B_{max}:

"ave(B_{max})", B_{max} value used in Eq. 2.21 is the average of B_{max} of each row of rough surface;

"max(B_{max})", B_{max} value used in Eq. 2.21 is the maximum of B_{max} of each row of rough surface;

"min(B_{max})", B_{max} value used in Eq. 2.21 is the minimum of B_{max} of each row of rough surface.

are used in the simplified multi-scale model in order to test the effect of B_{max} on the relations between A^* and P^*.

Solutions of the FE model of both isotropic and anisotropic surfaces lie between two limit solutions, i.e., min(B_{max}) and max(B_{max}). As the load P^* (or contact area A^*) increases, the FE solution transits from min(B_{max}) curve to max(B_{max}) curve. This may be explained by
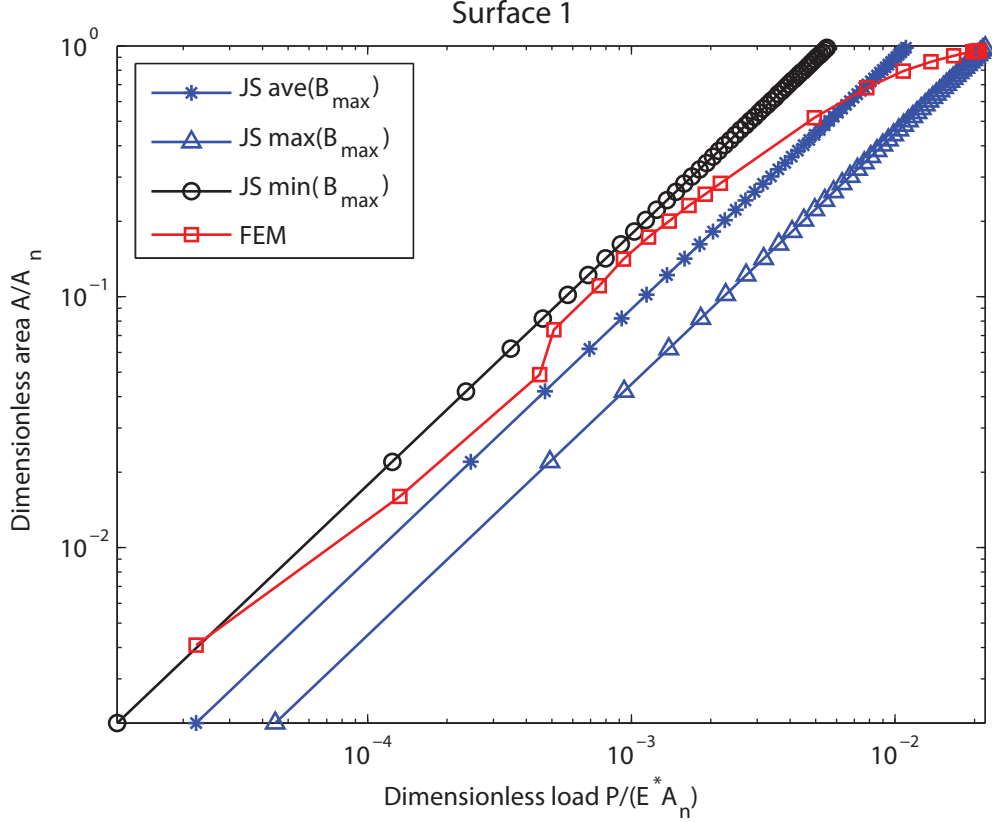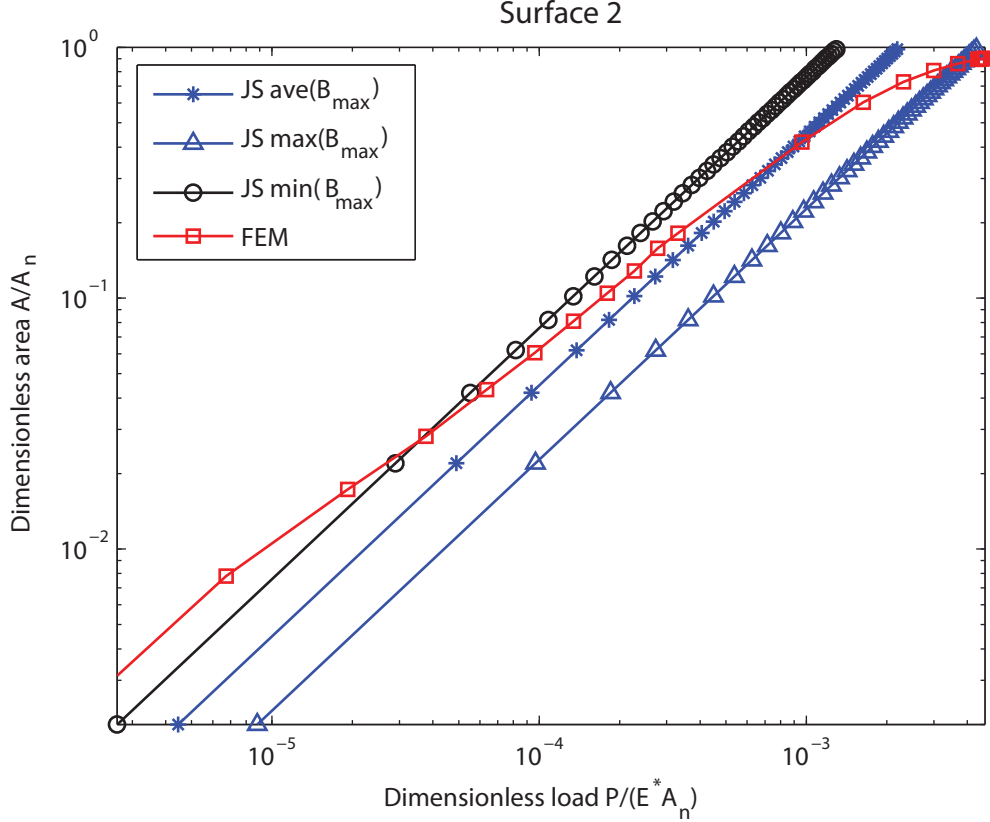
Figure 2.4: Contact area-load relation of surface 2 predicted by simplified multi-scale models [34] with different definition of B_{max}.

the following reasons: The definition of B is the ratio of the amplitude Δ to the wavelength λ. After the Fourier transformation of the 3D isotropic rough surface heights, we may have stacks of isotropic sinusoidal surfaces with different values of B. Assume we have two cross-sections of 3D isotropic sinusoidal surfaces with different values of B, i.e., B_1 and B_2. The wavelength, λ, of both sinusoidal waves are the same. The total load, needed to flatten those surfaces, is dependent on the B. Thus, the sinusoidal surfaces with the larger value of B have larger resistance to the deformation. Consequently, at the beginning of rough surface contact, i.e., low load conditions, a majority of deformation is due to the components of sinusoidal surfaces with smaller value of B. That is why the relation between A^* and P^* with $\min(B_{max})$ matches the solution of the FE model at the low load condition for both isotropic and anisotropic cases. As the load P^* increases, more and more sinusoidal components have been flattened. At the point of complete contact, the sinusoidal component with the largest

29

B, i.e., $\max(B_{max})$, is finally flattened. That is why when the $A^* = 1$, prediction of P^* by the simplified multi-scale model with $\max(B_{max})$ has a good agreement with that of the FE model. The two limiting solutions, i.e., $\min(B_{max})$ and $\max(B_{max})$, can exactly predict the asymptotic solutions at the early and complete contact when rough surfaces are isotropic, i.e., surface 1. For the anisotropic surfaces, i.e., surface 2, small mismatches can be found. This may due to the fact that the simplified multi-scale model is based on the isotropic assumption.

2.5   Conclusion

Some important statistical, multi-scale and semi-numerical models are discussed in this chapter. The statistical (the GW, Nayak, asymptotic BGT and CGP), the simplified multi-scale, Eq. 2.21, models and Ciavarella et al's model are compared to the finite element model. Conclusions drawn from the above comparison can be generalized as:

(1) Statistical models are only valid for extremely small load conditions which has already been accepted. Numerical results shown in Figs. 2.1 and 2.2 cannot prove it because the FEM solution is not accurate at low load conditions. The limited capability of the FEM model will be discussed in the following chapter.

(2) Except for adjacent asperity interaction, asperity coalescing may have even larger effect on the relation between A^* and P^*. The difference between Ciavarella et al.'s model with and without asperity coalescing can be found in Afferrante et al's paper [77]. Clearly, the accuracy of the one including the effect of asperity coalescing increases dramatically. Unfortunately, Afferrante et al's solution is not included in the above comparison because it is too difficult to recreate within the scope of this work

(3) The effect of the anisotropic nature of rough surfaces considerably influences the accuracy of all the elastic rough surface contact models, especially the statistical models.

Chapter 3

Finite element method

As the computational capabilities have become cheaper and more powerful, more and more efforts have been placed on the application of deterministic numerical methods in the simulations of rough surface contact. Due to the fact that it is not easy (sometimes impossible) to obtain the accurate contact area data from the experimental results, numerical solutions have always been treated as "exact" even though it definitely deviates from real solutions because of discretized and round off error. The *finite element method* (FEM) and the *boundary element method* (BEM) are two popular methods used in rough surfaces contact simulation.

Comparing to the massive usage of the BEM in the research of rough surface contact, the application of the FEM (especially 3 dimensional rough surfaces analysis) starts to appear just at the beginning of this century. Komvopoulos and Choi [59] may be the first to applied the FEM to rough surface contact. However, their finite element (FE) model was restricted to plane-strain problem. Rough surface is modeled by uniformly distributed cylindrical asperities and it is not real rough surface. As the storage capacity and computation speed increase, solving a million nodes model is no longer as much of a challenge. Thanks to the parallel computation technique, the computational time is dramatically saved by running the simulation in super computers with multiple cores. Hyun et al. [60, 61] and Pei et al. [62] applied the FEM in elastic and elastic-plastic rough surface contact with nearly one million nodes, respectively. Similar analysis have also been done by Sahoo and Ghosh [63], Walter and Mitterer [64], Yastrebov et al [65], Bryant et al [66], Olshevskiy et al [67] and Megalingam and Mayuram [68]. Additionally, Thompson [69] studied thermal contact resistance between contacting rough surfaces using the commercial software ANSYS$^{\text{TM}}$. Timzer [70] studied the

thermomechanical contact between randomly rough surfaces. A complete literature review of the development and application of the FEM in rough surfaces contact is provided by Thompson and Thompson [36].

In the current work, a FE model of rough surface contact is built and excuted using the commercial software ANSYS$^{\text{TM}}$. The FE modeling in ANSYS$^{\text{TM}}$is achieved by using the APDL language [71]. The advantage of using APDL language instead of the GUI operation is that the input parameter can be easily adjusted and data and solutions of the FE model can be easily accessed and exported.

3.1 Surface modeling

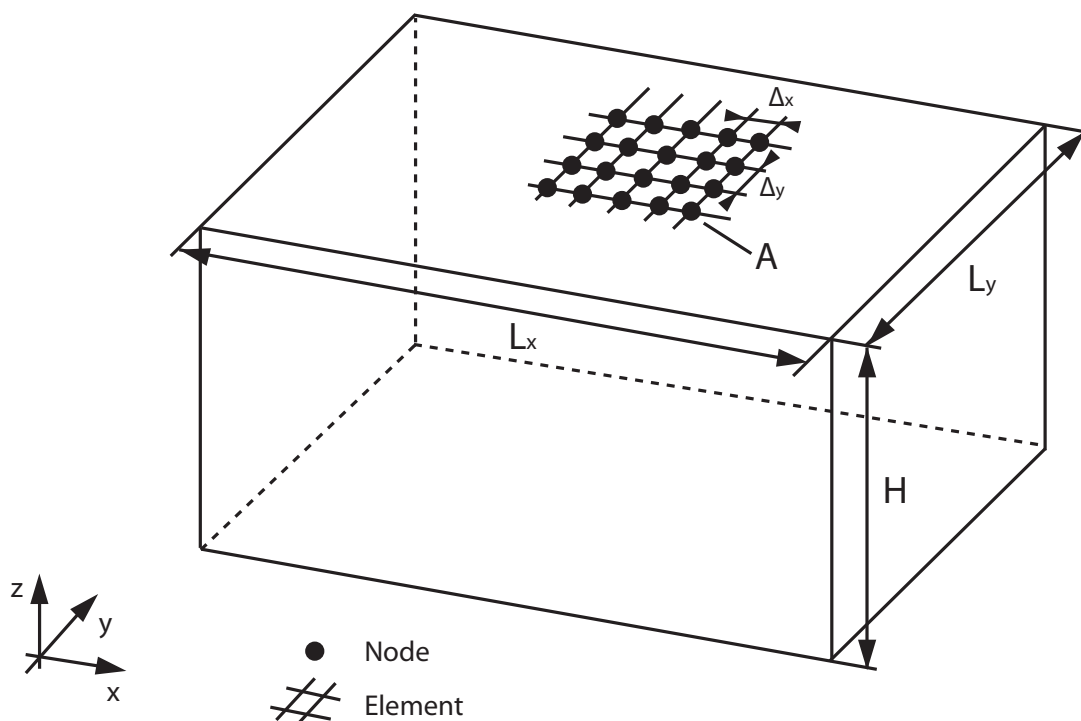Figure 3.1: Schematic representation of uniformly meshed elastic solid with smooth surface (only the mesh on the nominal contact surface are visible).

Generally, the rough surfaces used in FEM analysis can be divided into computer-simulated surfaces [60, 62, 63, 70, 68] and real surfaces[64, 65, 66, 67, 69]. No matter what kind of rough surfaces data are used, meshing the rough surfaces and its sub-surface is always

32

a challenging task. Currently, two methods have been widely used in the above references, namely, *moving nodes* and *direct surface generation.*

Moving Nodes [60]

Assume we have a rectangular volume with a flat top surface of $L_x \times L_y$ and a thickness, H (see Fig. 3.1). This volume has been discretized using a uniform mesh. Node A is locating on the boundary or inside the volume, with the coordinates (x, y, z). Coordinate z is measured from bottom surface. In order to obtain the rough surface $h(x, y)$ on the top surface and to prevent the moving procedure from distorting the shape of the elements, we move the node A by

$$\Delta z = h(x, y) \left(\frac{z}{H} \right)^a$$

only along the z direction. a is a constant defined by users. H is the dimension measured between the top and bottom surface. Nodes on the top surface will move by the amount of $h(x, y)$ and the coordinate change along the z direction drops exponentially to zero until the changes reach the nodes on the bottom surface.

Direct Surface Generation

The idea of this method is to directly generate the rough surface through the sampling point cloud, then the bottom-up technique [69] is used to create a volume for meshing. Four neighboring sampling points can form a Coon's patch [71] (those sampling points are not co-planar). By using the Boolean operation, we can create the entire rough surface. However, great care should be placed when using Boolean operation, especially in ANSYS$^{\text{TM}}$, to avoid failure.

Due to the fact that direct surface generation is not robust in ANSYS$^{\text{TM}}$, we choose the method of moving nodes as the strategy for generating the rough surface mesh in the current work. Usually, meshing of a solid with a rough surface results in more than $200,000$ nodes, and therefore moving all the nodes may cost considerable operation time during pre-processing. In the current work, only nodes on the top surface are moving.
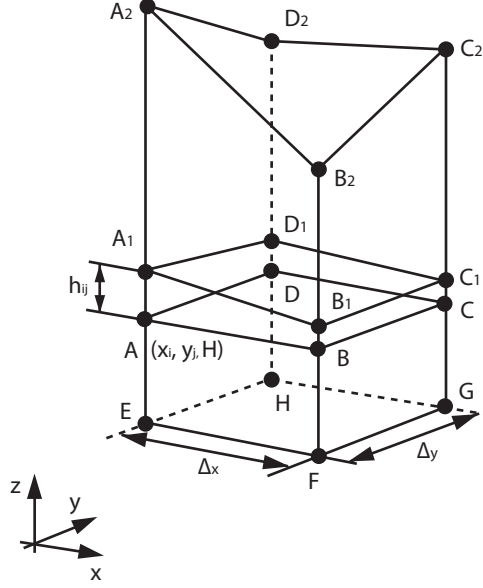
Figure 3.2: Schematic representation of a badly distorted rough surface element.

The elastic solid, see Fig. 3.1, is meshed uniformly at intervals Δx and Δy along the x and y directions. Δx and Δy are the resolutions of the profilometer along the x and y directions. Since only the nodes on top surface are moved, the value of $\Delta z(x, y)$ equals $h(x, y)$. If the amount of moving (h_{ij}) at node (x_i, y_j) is larger than the dimension of interval Δx and Δy, the shape of the element may be badly distorted (see element $A_2 B_2 C_2 D_2 EFGH$ in Fig. 3.2). In order to avoid distorted elements, a rough surface is selected for which the $\max(|h|)$, the maximum absolute value of the rough surface height, is less than the mesh interval $(\min(\Delta x, \Delta y))$. Fig. 3.3 and 3.4 illustrates the details of the mesh of surface 1 and surface 2 when the procedure of the moving nodes is achieved in ANSYS$^{\text{TM}}$. When $\max(|h|)$ of the rough surface is larger than the $\min(\Delta x, \Delta y)$, all the nodes need to be moved, as was done in [60], in order to avoid element distortion.

Size of the rigid flat is chose to be much larger than that of the nominal contact area of rough surface in this study.
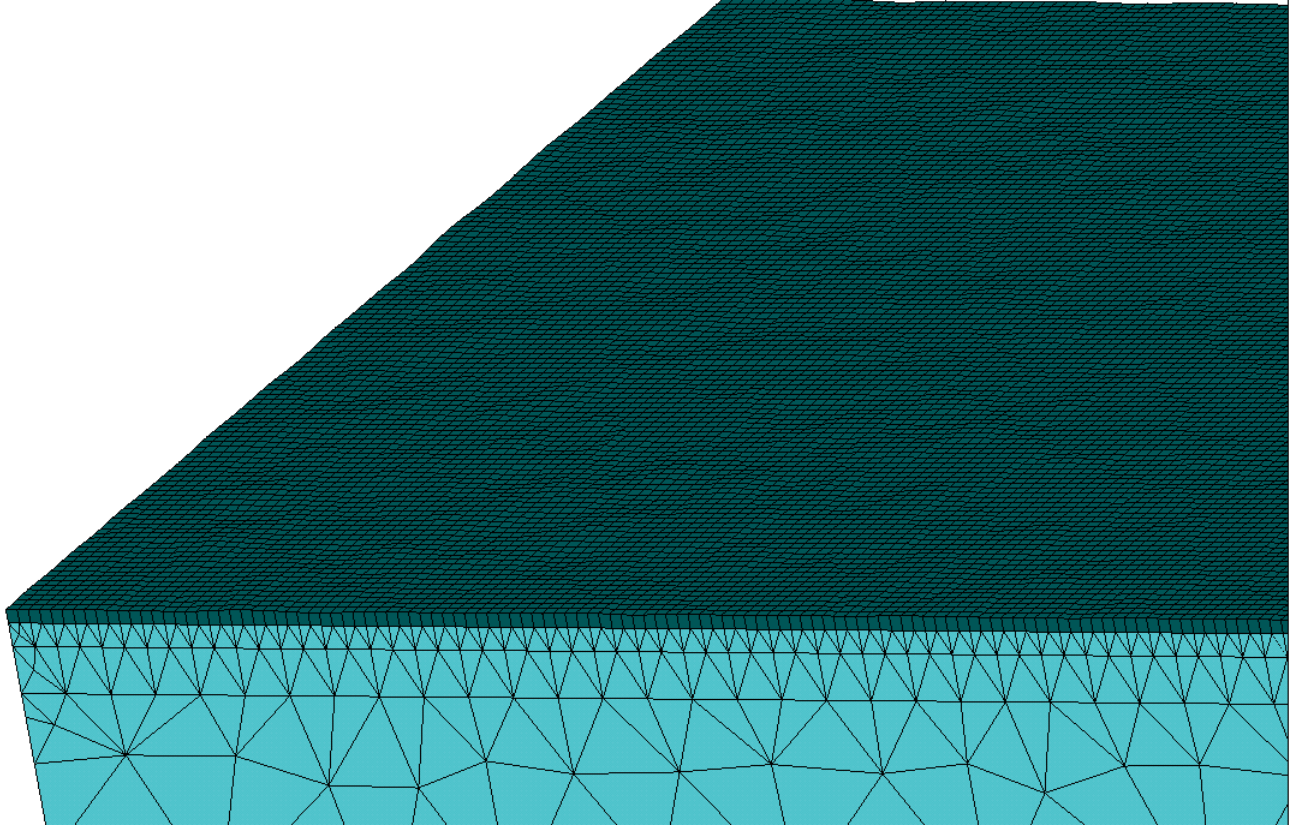
Figure 3.3: Details of surface mesh of surface 1.

3.2 Boundary condition and effect of thickness

It is easy to achieve the assumptions namely, cyclic symmetry and infinite thickness, declared in the beginning of this chapter in ANSYS$^{\text{TM}}$.

For the former one, i.e., cyclic symmetry, we should couple all the degrees of freedom (D.O.F) of nodes on the opposite side surfaces. Fig. 3.5 shows the top view of the infinite rough surface consists of finite rough surface cells. All the rough surface cells are the same and only one of them has been modeled in ANSYS$^{\text{TM}}$. Points A and B are two nodes on the opposite side surfaces 1 and 2, respectively, and share the same coordinates on cyclic symmetric boundary. During each iteration, ANSYS$^{\text{TM}}$ calculates the nodal displacement at A in the x, y and z directions, i.e., $U_x(A), U_y(A), U_z(A)$ and assigns the same U_x, U_y and U_z values to node B. Similarly, the values of U_x, U_y and U_z are enforced to be the same at
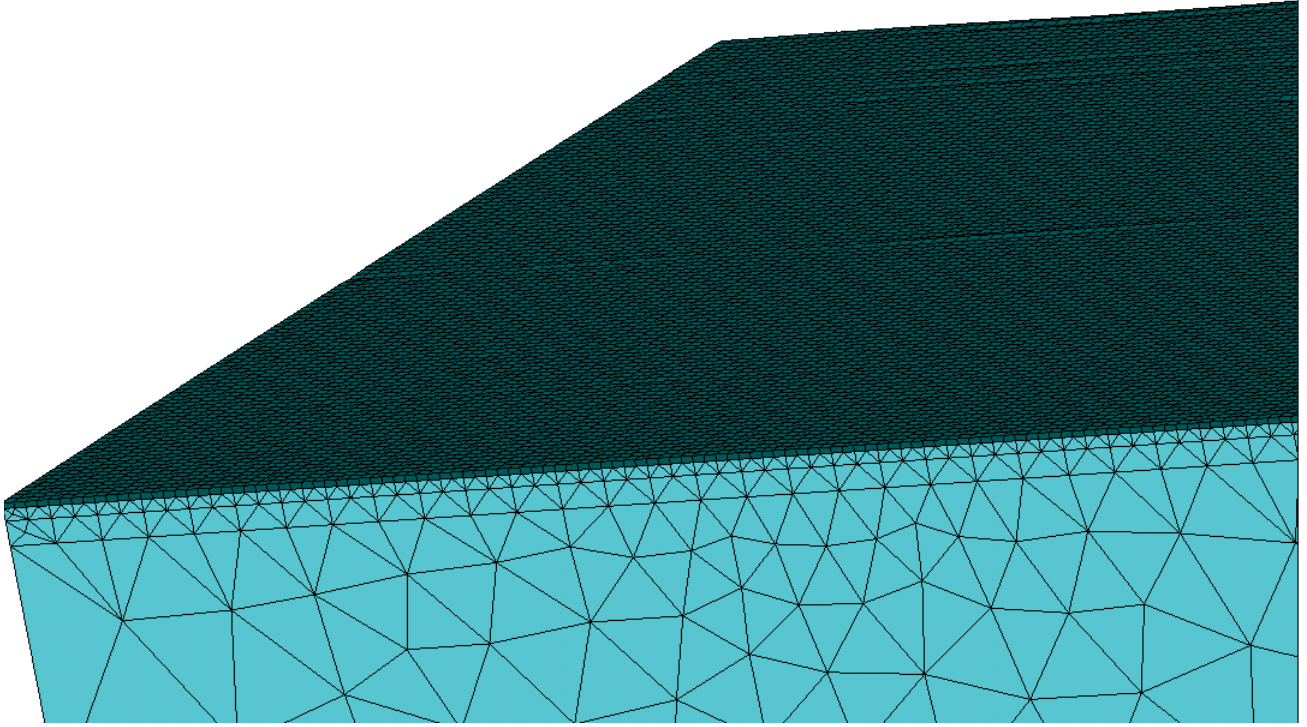
Figure 3.4: Details of surface mesh of surface 2.

nodes C and D. In the current work, only *weak-coupling* is applied in the FE model, i.e., $U_x(A) = U_x(B)$ and $U_y(C) = U_y(D)$.

Besides the cyclic symmetric boundary condition (Fig. 3.6(a)), other two boundary conditions namely, the constrained side surfaces (Fig. 3.6(b)) and free side surfaces (Fig. 3.6(c)) are also studied in the current work. All the nodal displacements on side surfaces are constrained in Fig. 3.6(b) and are free in Fig. 3.6(c).

The contact area to load $(A^* - P^*)$ and the contact area to surface separation $(A^* - (d')^*)$ relations from the FE models with the above three boundary conditions are obtained in ANSYS$^{\text{TM}}$ and compared in Figs. 3.7-3.10. It is surprising to find that the A^* to P^* and A^* to $(d')^*$ relations of the three different boundary conditions are almost identical. This phenomenon may result from the negligible displacements along the in-plane directions, x and y, compared to that in the vertical direction during the rough surfaces contact.
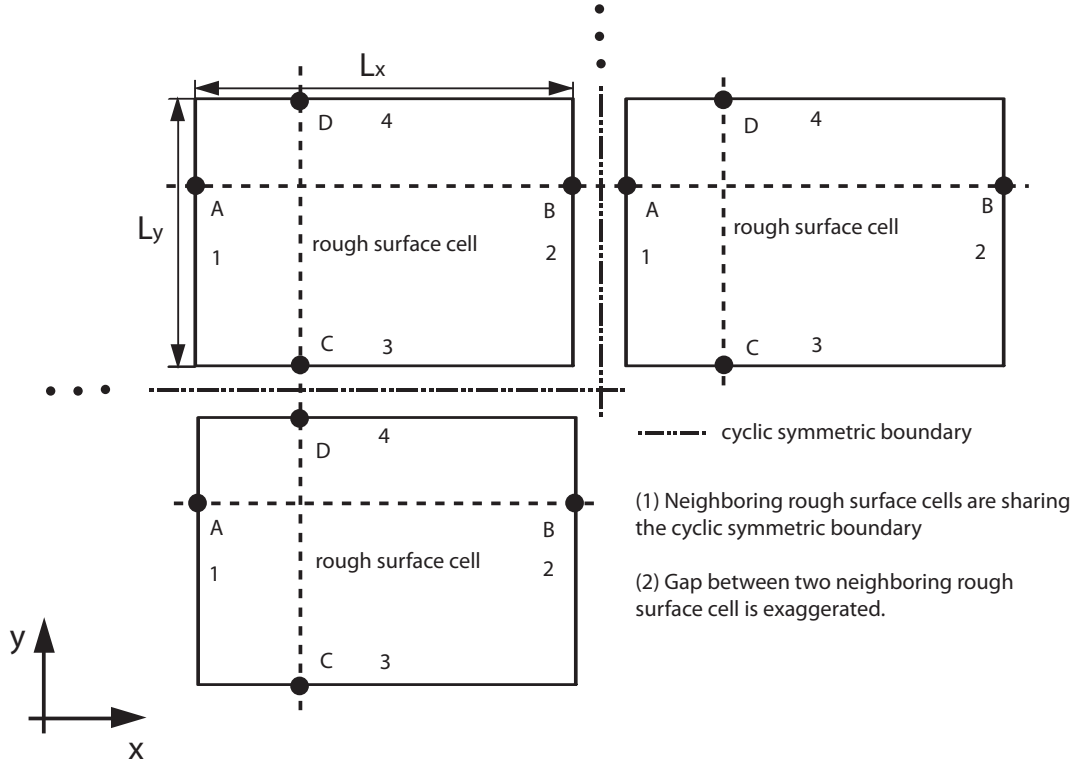
Figure 3.5: Schematic representation of cyclic symmetry and displacement coupling

The second assumption is infinite thickness and in other words: the contact results, at least contact load, P^*, area, A^*, and surface separation, $(d')^*$, relations, should be independent of thickness, H. We tested the FE models with different values of thickness namely, $H = 0.5L_x$, $H = L_x$ and $H = 5L_x$. If we represent the thickness in the function of RMS roughness σ, we have: surface 1, $H = 308.88\sigma$, $H = 617.76\sigma$ and $H = 3088.80\sigma$, surface 2, $H = 2041.6\sigma$, $H = 4082.6\sigma$ and $H = 2041.6\sigma$. The corresponding contact area to load relations are plotted in Figs. 3.11-3.14. We can conclude from Figs. 3.11-3.14 that the contact load, P^*, area, A^*, and surface separation, $(d')^*$, relations are independent of the thickness H, at least, when thickness is larger than $0.5L_x$.

3.3 Results and discussion

In the above section, we have shown that the A^* to P^* and A^* to $(d')^*$ relations predicted by the FE models with three different boundary conditions have good agreement (see Figs.

Figure 3.6: Schematic representation of boundary conditions: (a) cyclic symmetry, (b) constrained side surfaces and (c) free side surfaces

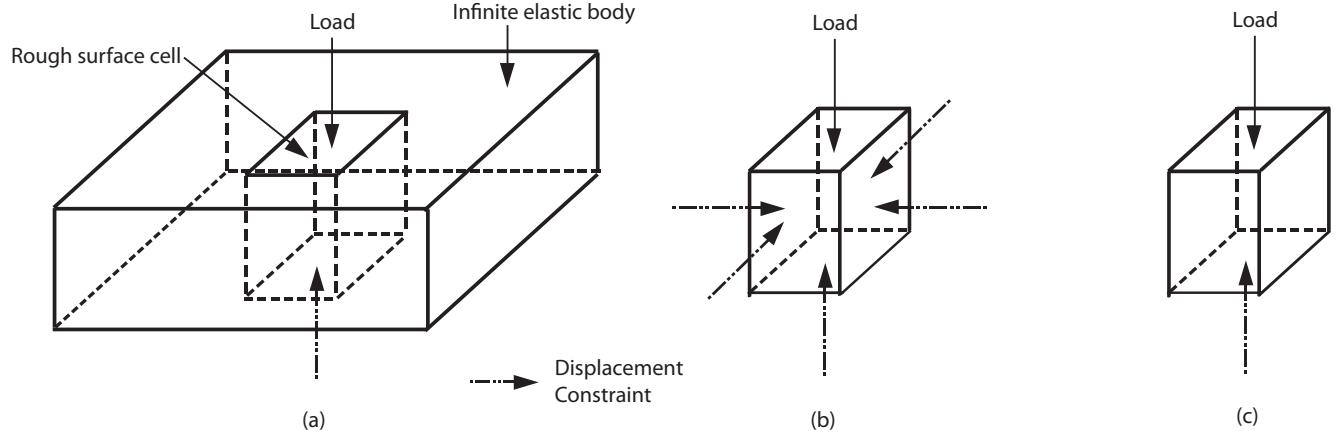3.7-3.10). Additionally, the A^* to P^* and A^* to $(d')^*$ relations are independent of thickness, H, when $H > 0.5L_x$ (see Figs. 3.11-3.14). The A^* to P^* solution used in the comparison in Chapter 2 is obtained by the FE models with free side surfaces boundary condition and $H = L_x$.

Fig. 3.15 and 3.16 illustrate the contact area and pressure distribution of surface 1 and surface 2 at different contact stages and are the solutions of the FE model with free side surfaces boundary condition and $H = L_x$. At the low contact force (see Fig. 3.15(a-b) and 3.16(a-b)), contact spots of asperities grow independently. At the medium load condition (see Fig. 3.15(c-d) and 3.16(c-d)), asperity coalescing becomes severe and independent contact spots form into contact patches with irregular shapes. At the high load condition (see Fig. 3.15(e-f) and 3.16(e-f)), only the not in contact spots grow independently. For the nearly isotropic surface, i.e., surface 1, shapes of the contact spots at the low load condition (a) and the not in contact spots at high load condition (e) are close to circular and ellipsoid. For surface 2, which shows a strong anisotropic nature, the shapes of contact spots at the low load condition (a) and the not in contact spots at high load condition (e) are more like long strips and ellipsoids.

38

The correlation between rough surface height distribution and pressure distribution can be found in Figs. 3.17 and 3.18 when complete contact is nearly achieved. Because the contact has not been reached complete, the correlation of surface 2 is not obvious.
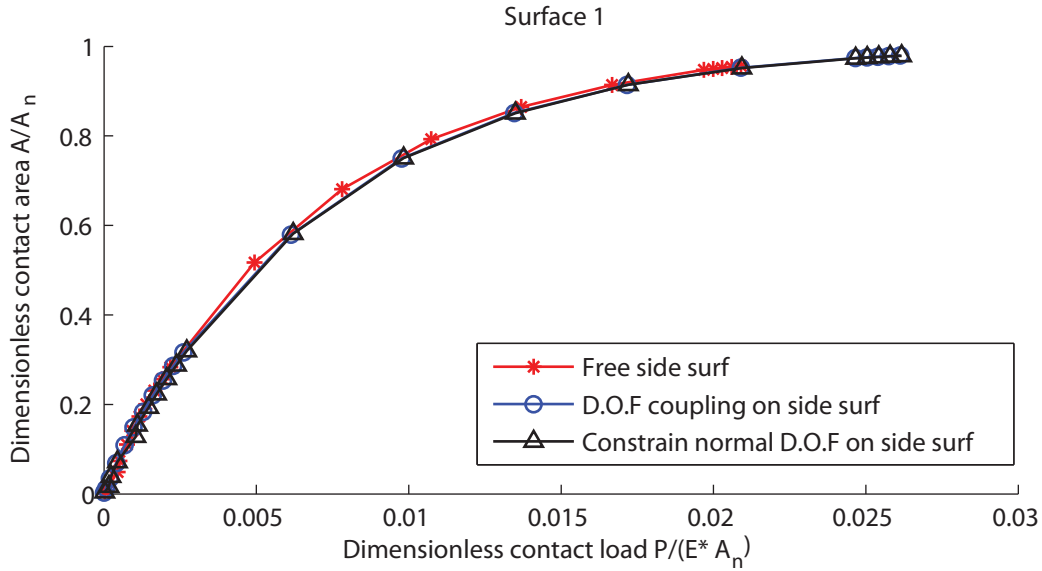
Figure 3.7: Dimensionless contact area A^* to dimensionless load P^* relation of surface 1. The FE models with different boundary conditions illustrated in Fig. 3.6.

3.4 Conclusion

Application of the finite element method is discussed in this chapter. The following conclusions may be drawn from the above discussion:

1. Pre-processing in the FEM is tedious and time consuming, especially during the meshing procedure.

2. According to the contact area to load results with different boundary condition, the FE model in this study is valid for periodic domain problem.

3. Global contact results (contact load, area and surface separation) relations are independent of the thickness of the substrate of the rough surface, at least when $H > 0.5L_x$.

39
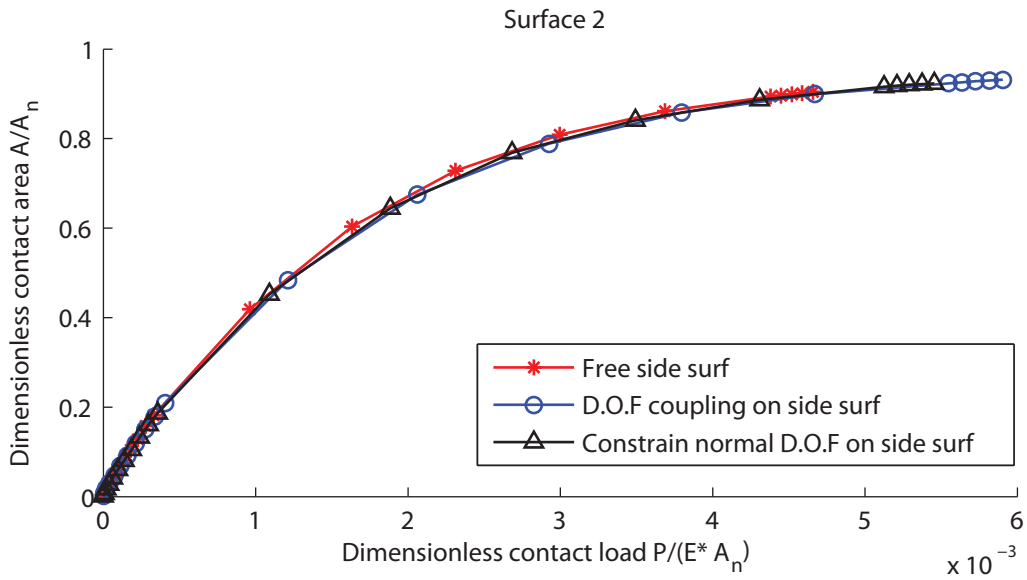
Figure 3.8: Dimensionless contact area A^* to dimensionless load P^* relation of surface 2.
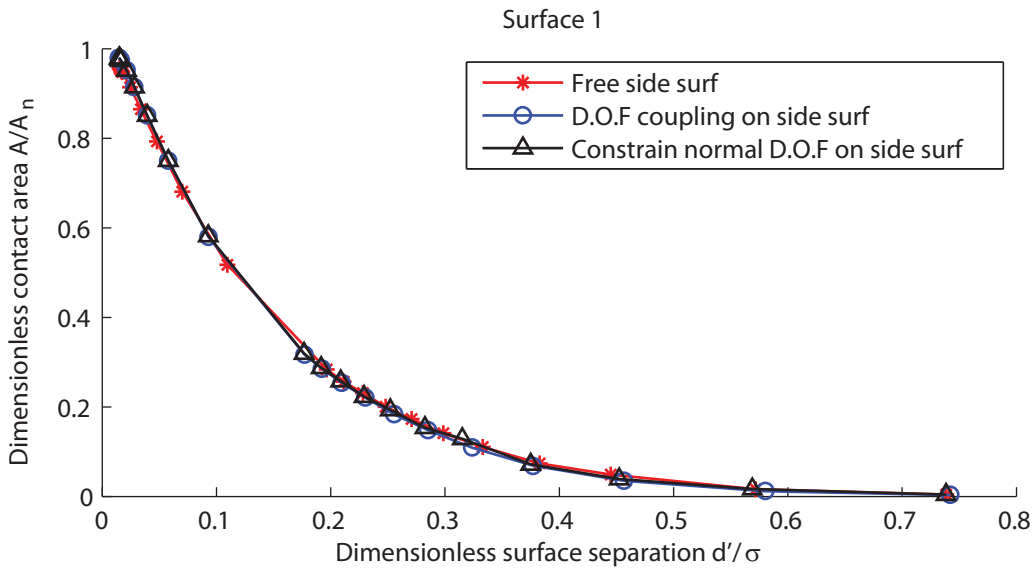
Figure 3.9: Dimensionless contact area A^* to dimensionless surface separation $(d')^*$ relation of surface 1.
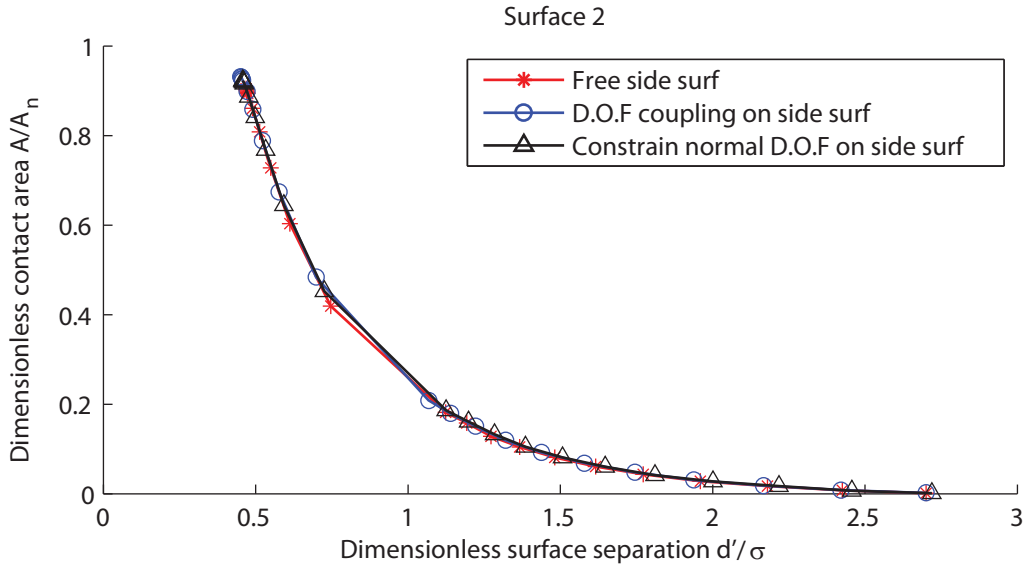
Figure 3.10: Dimensionless contact area A^* to dimensionless surface separation $(d')^*$ relation of surface 2.
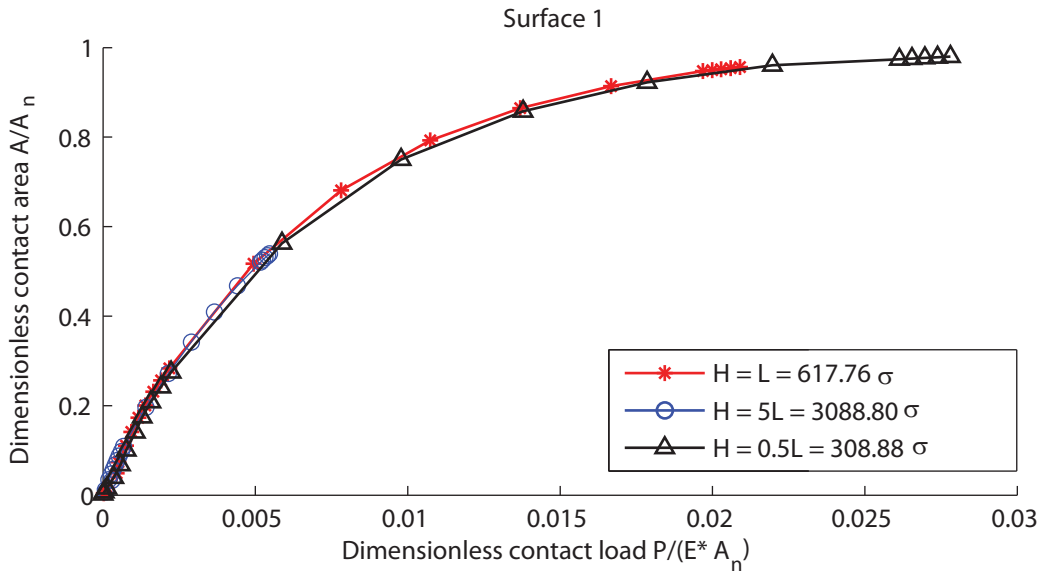
Figure 3.11: Dimensionless contact area A^* to dimensionless load P^* relation of surface 1. Value of thickness: $H = 0.5L_x,\ L_x,\ 5L_x$.
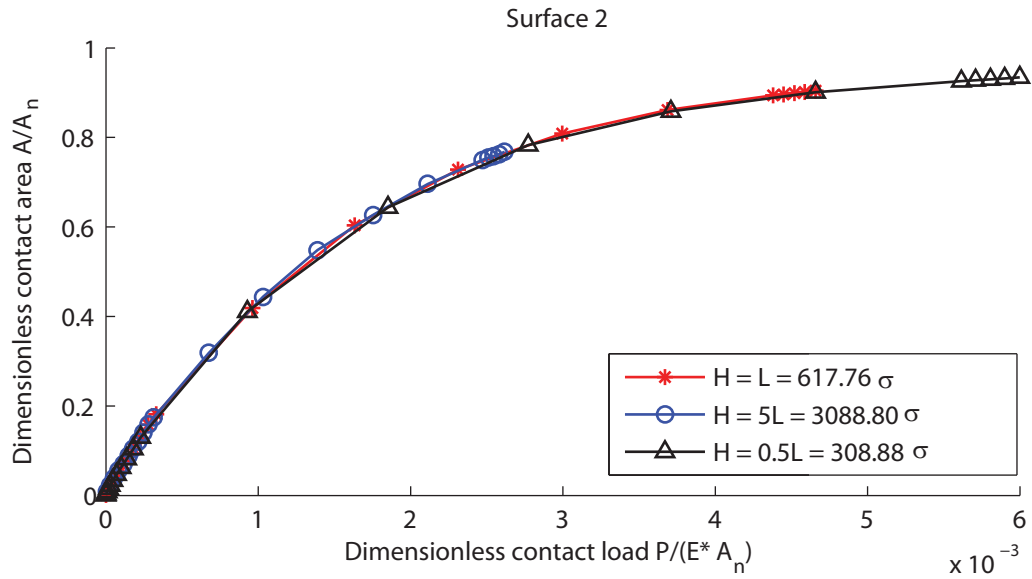
Figure 3.12: Dimensionless contact area A^* to dimensionless load P^* relation of surface 2. Value of thickness: $H = 0.5L_x$, L_x, $5L_x$.
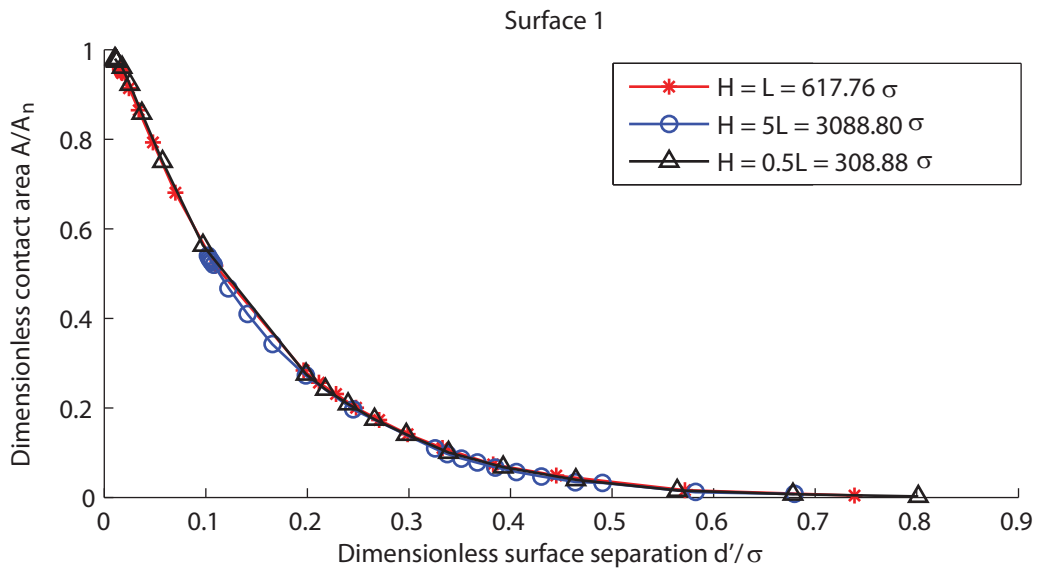
Figure 3.13: Dimensionless contact area A^* to dimensionless surface separation $(d')^*$ relation of surface 1. Value of thickness: $H = 0.5L_x$, L_x, $5L_x$.
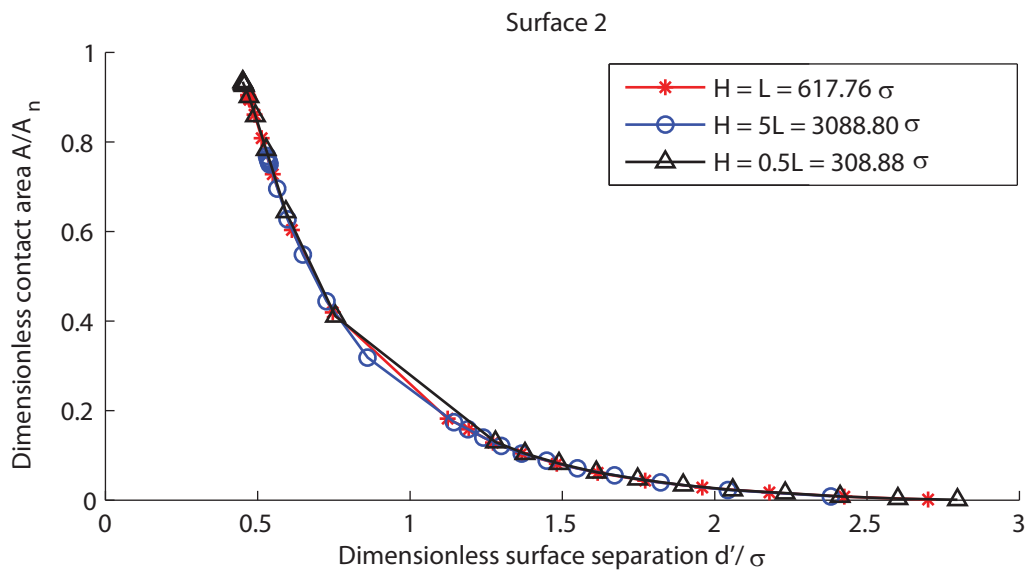
Figure 3.14: Dimensionless contact area A^* to dimensionless surface separation $(d')^*$ relation of surface 2. Value of thickness: $H = 0.5L_x$, L_x, $5L_x$.
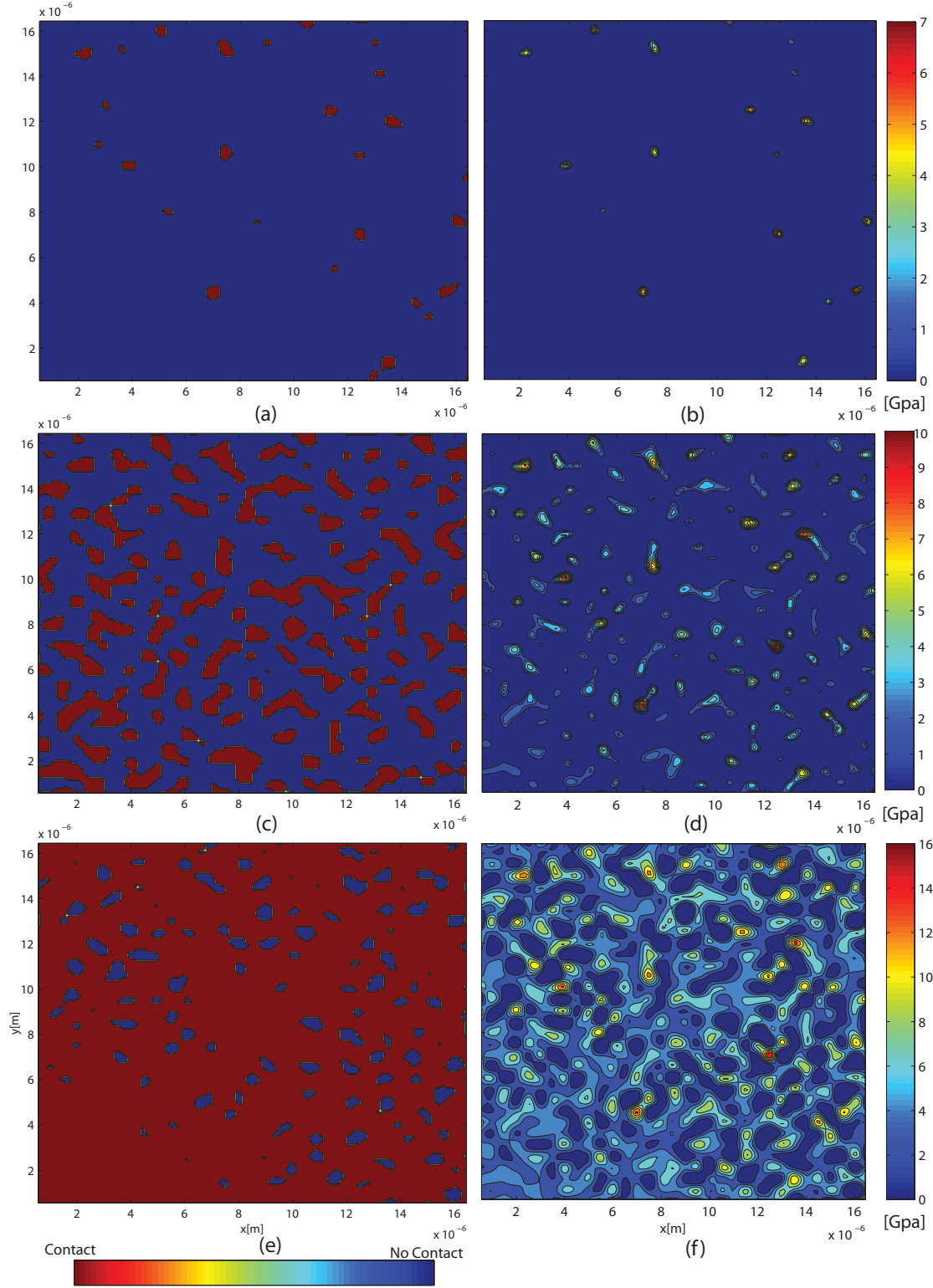
Figure 3.15: Contact area contours and contact pressure distribution of surface 1 when contact load is light(a-b), medium(c-d) and high(e-f). Light load: $P^* = 4.49 \times 10^{-4}$, $A^* = 0.0489$. Medium load: $P^* = 0.00218$, $A^* = 0.283$. High load: $P^* = 0.00438$, $A^* = 0.948$.
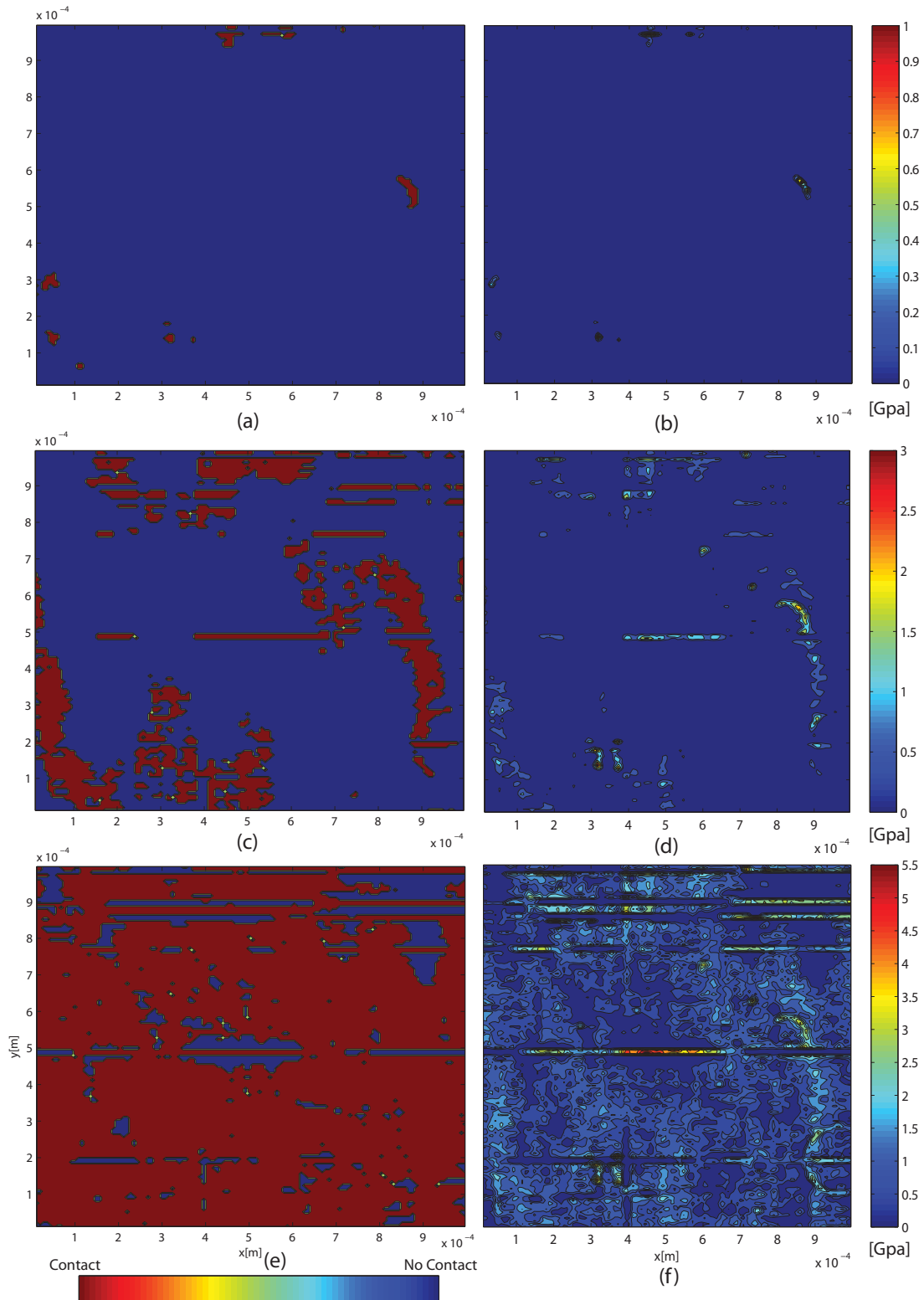
Figure 3.16: Contact area contours and contact pressure distributions of surface 2 when contact load is light(a-b), medium(c-d) and high(e-f). Light load: $P^* = 1.91 \times 10^{-5}$, $A^* = 0.0173$. Medium load: $P^* = 9.62 \times 10^{-4}$, $A^* = 0.419$. High load: $P^* = 0.00438$, $A^* = 0.894$.
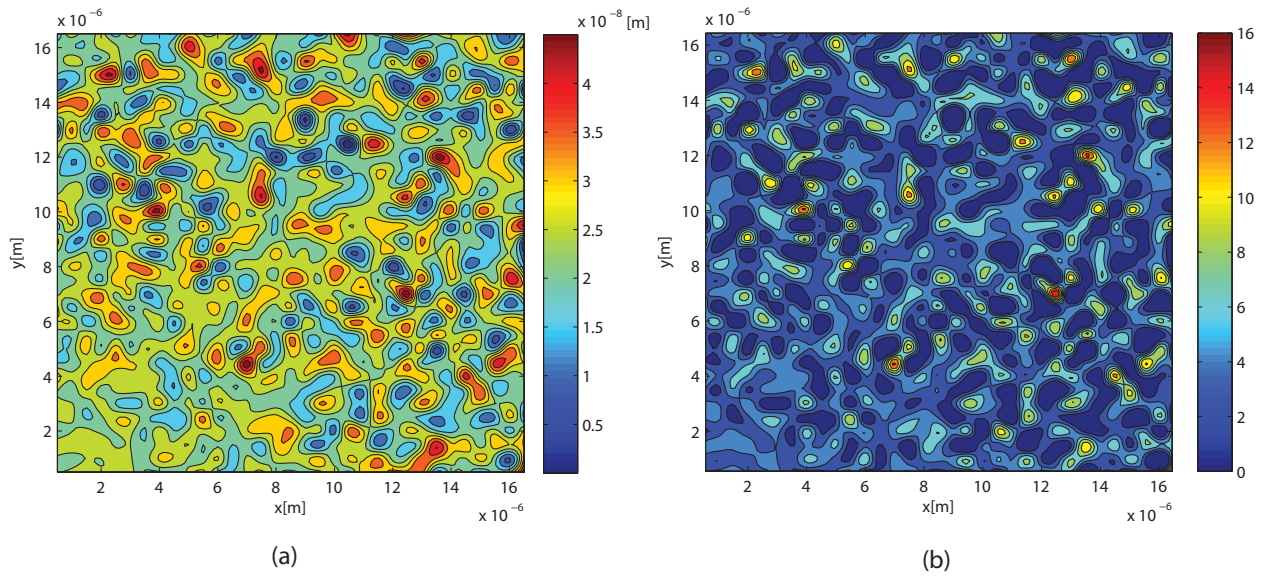
Figure 3.17: Correlation of rough surface geometry (a) and pressure distribution (b) of surface 1.
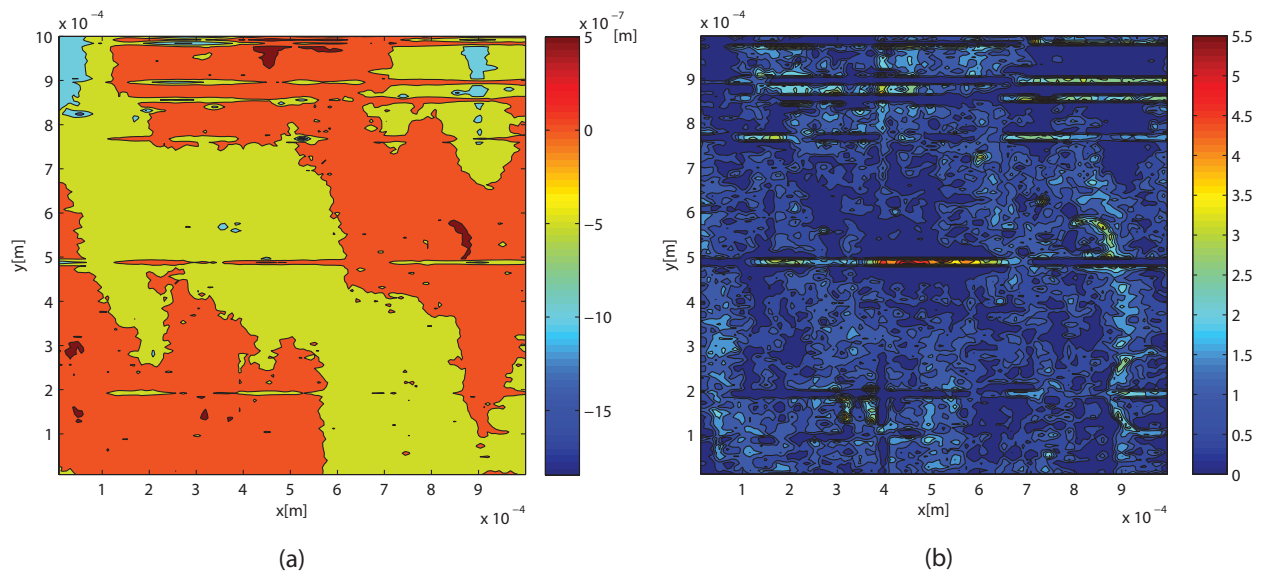
Figure 3.18: Correlation of rough surface geometry (a) and pressure distribution (b) of surface 2.

Chapter 4

Boundary element method

Rough surface modeling is always the biggest problem when the FEM is chosen to simulate the contact. The accuracy of the FEM can be directly affected by the mesh quality. Each potential contact geometrical entity, i.e., asperities, and its subsurface needs to be discretized using a highly refined mesh. Usually, for a small or medium size rough surface contact problem, the ultimate number of nodes required to obtain an "accurate" result is on the order of millions or even more [36].

The BEM, however, has a natural advantage in solving rough surface contact problem. Based on the help of the influence function, only the boundary of the problem domain needs to be discretized, i.e., more nodes are saved to discretize the rough surface model with a finer mesh. Additionally, the solution of stress and displacement within the domain are more accurate than that on the boundary [37]. While the BEM has long been criticized for its dense, full rank, non-symmetrical coefficient matrix (symmetrical and sparse in the FEM) created during the formulation, thus the storage of the coefficient matrix and solving of the whole system becomes a challenging task for the personal computer (PC) with a limited storage capacity or even the workstation. Looking back into the history of the development of the BEM, there is a long period, during which only thousands of D.O.Fs can be solved by the BEM due to the limited storage capacity of typical computational device [37, 38]. However, as the source point is closer to the boundary of the domain, the solution may become less accurate due to the singular integration. Thus the subsurface stress distribution, which is close to the rough surface, may not be as accurate as expected. The first disadvantage, dense coefficient matrix, can be overcome by using a fast multipole boundary element method [38].

Even though the BEM can handle more rough surface sampling points than the FEM, it is always unfeasible to include an entire fully detailed sampled surface in any numerical method. Generally, only a part of the surface data is collected by a profilometer with relatively fine resolution down to the nano scale. The sampled area may result in millions of sampling points and not to mention the entire rough surface. In order to overcome both computation and storage capacity limits, we assume:

1. *Rough surface contact pair, including rough surface and rigid flat, is cyclicly symmetric along x and y*(Fig. 3.5). Each rough surface cell in Fig. 3.5 represents the same sampled rough surface which cyclicly distributes along the x and y directions.

2. *Nominally elastic flat rough surface has an infinite depth.*

Assumption 1 enables the analysis of rough surface contact to restrict within a small sampled area with fine resolution and surface data to reveal the multi-scale structure of rough surfaces as much as possible. Additionally, assumption 1 dramatically decreases the computation time and storage memory. Assumption 2 actually is a byproduct of assumption 1, since the in-plane dimensions of the sampled surface is negligible compared to the in-plane dimensions of entire rough surface. The combination of assumptions 1 and 2 are equivalent to the assumption of an *elastic half-space*.

In the rest of this chapter, applications of the BEM in modeling the rough surface contact are discussed thoroughly. A special kind of the BEM is derived by adopting some essential assumptions. Methods of solving the nonlinear boundary integral equation are discussed. Additionally, fast algorithms for deformation integral are also introduced. Solutions, the relations of contact area and load, of the BEM are compared to that of the FE model.

4.1 Boundary integral equation

Boundary integral equation of three dimensional elastostatic problem is [37]

$$u_i(p) + \iint\limits_{\Omega'} T_{ij}(p,Q)u_j(Q)\,dS(Q) = \iint\limits_{\Omega'} U_{ij}(p,Q)t_j(Q)\,dS(Q), \quad p,Q \in \Omega' \qquad (4.1)$$

where u and t indicate the surface displacement and surface traction on boundary Ω'. T_{ij} is the traction kernel denotes the traction at point p which lies on a certain plane due to the unit point load at point Q. U_{ij} is the displacement kernel denotes the displacement of point p due to the unit point load. T_{ij} and U_{ij} are derived from Kelvin fundamental solution of an infinite solid. $i, j = x, y$ and z.
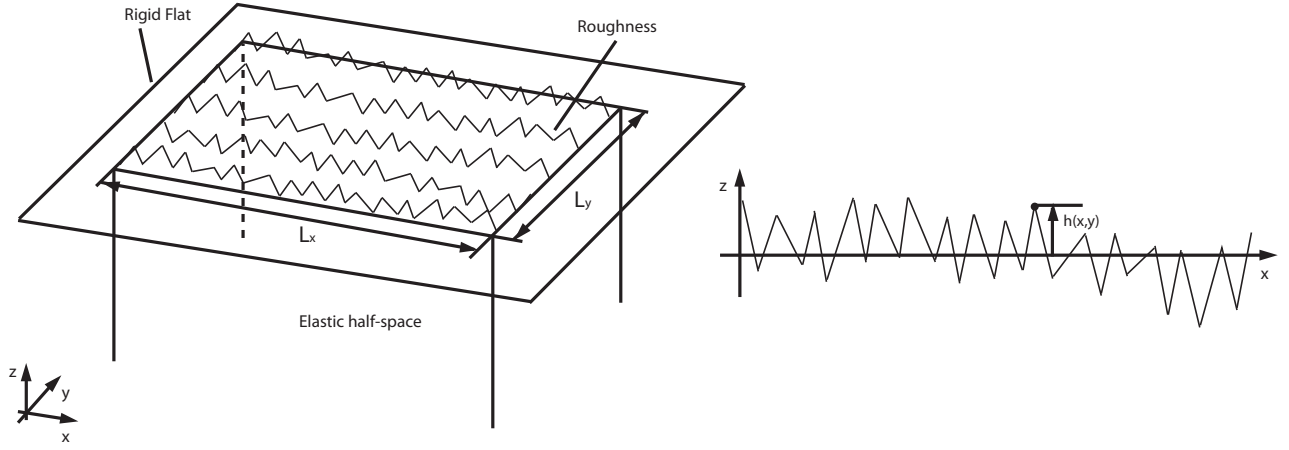
Figure 4.1: Semi-infinite contact body and its rough boundary.

Let us consider a special case, in which contact occurs between one nominally flat rough surface and one rigid flat, see Fig. 4.1. The body with the rough surface is assumed to be a semi-infinite body with the boundary $z = h(x, y)$ which is measured from mean level. The rigid flat has a finite dimension in the x (L_x) and y(L_y) direction, see Fig. 4.1. Consequently, boundary Ω' in Eq. 4.1 now indicates the rough surface which is the only boundary of the semi-infinite contact body. Commonly, the height of the rough surface, h, is negligible when comparing to the in-plane dimension of the contact body, e.g., L_x and L_y. Thus we can further assume that $z = 0$ plane can approximate the boundary of semi-infinite contact body.

Define domain Ω as part of domain Ω' which coincides with the in-plane region of rigid flat: $\{(x, y) \in \Omega | 0 \leq x \leq L_x, 0 \leq y \leq L_y\}$. The traction components within the region $\Omega' - \Omega$ is zero, i.e., $t_x(Q) = t_y(Q) = t_z(Q) = 0, Q \in \Omega' - \Omega$. Because the contact is frictionless, thus $t_x(Q) = t_y(Q) = 0, Q \in \Omega$. $u_x(Q)$ and $u_y(Q)$ are negligible comparing to the dominant

49

deformation $u_z(Q)$ within the contact region Ω. Based on above assumptions, Eq. 4.1 can be rewritten as

$$u_z(p) + \iint\limits_{\Omega'} T_{33}(p, Q)u_z(Q)\, dS(Q) = \iint\limits_{\Omega} U_{33}(p, Q)t_3(Q)\, dS(Q), \quad p, Q \in \Omega \qquad (4.2)$$

T_{33} is the traction kernel indicating the value of traction in z direction at point p, i.e., $t_3(p)$, due to the unit displacement in z direction at point Q, i.e., $u_3(Q)$. Point p and Q are two points inside the infinite body according to Kelvin fundamental solution. In our special case, Eq. 4.2, p and Q are all on the boundary Ω. From a physical perspective, point Q cannot "feel" any load due to the unit displacement at point p, because of lack of continuum medium to transfer the traction. As a results of above explanation, $T_{33} = 0$ within the boundary Ω and Eq. 4.2 can be further simplified as

$$u_z(p) = \iint\limits_{\Omega} U_{33}(p, Q)t_3(Q)\, dS(Q), \quad p, Q \in \Omega \qquad (4.3)$$

Eq. 4.3 is the original equation which is wildly used in modeling the contact problem in tribology, especially contact mechanics with smooth interfaces [32]. The main assumptions used in deriving the Eq. 4.3, the reduced form of three dimensional boundary integral equation of elastostatic problem, are:

(1) One contact solid with a rough boundary is assumed to be a semi-infinite body with the simplified boundary $z = 0$;

(2) Rough surface displacements along x and y are negligible comparing to that in z, i.e., $u_x \ll u_z$ and $u_y \ll u_z$;

(3) The contact is frictionless.

4.2 Formulation of rough surfaces contact problem

x-y plane of coordinate system coincides with the mean level of rough surface. d is the surface separation measured between rigid flat and mean level. The origin of the coordinate system is placed at the bottom left corner of the Ω domain. Ω is discretized a into uniform 2D grid such that

$$\{(x,y) \in \Omega | x_i = (i-1)\Delta_x, y_j = (j-1)\Delta_y, i = 1, ..., n_x, j = 1, ..., n_y\}$$

with element size $\Delta_x \times \Delta_y$. Δ_x and Δ_y are also the sampling resolutions of rough surface data in x and y directions. n_x and n_y are number of the sampling points along x and y directions.
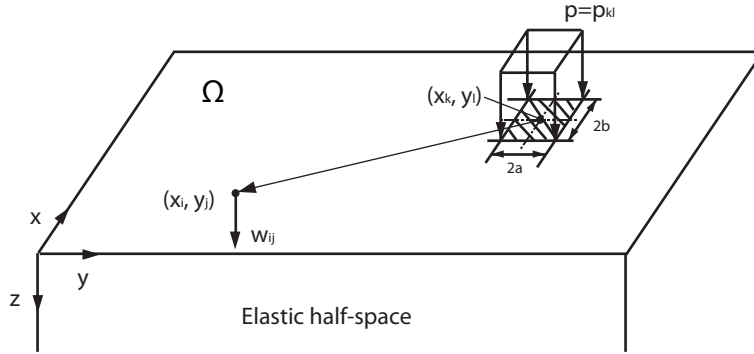
Figure 4.2: Schematic representation of displacement due to uniform pressure distribution.

Assume a piece-wise constant contact pressure (same as traction t_3) distribution p within the domain Ω, see Fig. 4.2, i.e., the pressure p within a rectangular cell (shaded area) , $2a \times 2b$ (same as $\Delta_x \times \Delta_y$) centered about point (x_k, y_l), has a constant value p_{kl}.

Rewriting Eq. 4.3 in a discretized form with commonly used symbols in contact mechanics, we have

$$w_{ij} = \sum_{(x_i,y_j)\in\Omega} \sum_{(x_k,y_l)\in\Omega} K_{ijkl}\, p_{kl} \tag{4.4}$$

where

$$K_{ijkl} = \iint\limits_{\Omega_c} U_{33}(x_i, y_j, x_k, y_l) \, dxdy, \quad (x_k, y_l) \in \Omega_c$$

w_{ij} and p_{kl} are the displacement and contact pressure along z direction at at boundary point (x_i, y_j), respectively. Ω_c is the domain of shaded cell centered about point (x_k, y_l). K_{ijkl} is called *influence coefficient* which derived by Love [39] and expression of K_{ijkl} can be found in Appendix B.

Define two sub-domains: I^c and I^{nc}. Points within domain I^c are in contact with rigid flat and are not in contact within I^{nc}.

The discretized governing equation of modeling the contact between a nominally flat rough surface and one rigid flat is

$$g_{ij} = \sum_{(x_i,y_j)\in\Omega} \sum_{(x_k,y_l)\in\Omega} K_{ijkl} \, p_{kl} + d - h_{ij}, \quad (x_i, y_j) \in \Omega, \quad (x_k, y_l) \in I^c \qquad (4.5)$$

where g_{ij} is the gap in z direction between rough surface and rigid flat at point (x_i, y_j). The boundary conditions for Eq. 4.5 are

$$p_{ij} \neq 0, \quad g_{ij} = 0, \quad \forall (x_i, y_j) \in I^c \qquad (4.6)$$
$$p_{ij} = 0, \quad g_{ij} \geq 0, \quad \forall (x_i, y_j) \in I^{nc}$$

4.3   Solver

Because the unknown in Eq. 4.5 is pressure p and the value of p within the non-contact region I^{nc} is zero according to the free-traction boundary condition 4.6. Eq. 4.5 only needs to be solved within region I^c. Venner and Lubrecht [40] suggested to use the matrix $\mathbf{D}$

$$D_{ms} = K_{ijkl}, \quad m = |i - k| + 1, s = |j - l| + 1$$

to replace the fourth order tensor K_{ijkl} due to the fact that influence coefficients K_{ijkl} is only dependent on the relative distance between (x_i, y_j) and (x_k, y_l). Then

$$\sum_{m=0}^{n_x-1} \sum_{s=0}^{n_y-1} D_{ms}\, p_{kl} = h_{ij} - d, \quad (x_i, y_j), (x_k, y_l) \in I^c \tag{4.7}$$

Because domain I^c is unknown before solving Eq. 4.7, an iterative method needs to be carried out and an initial guess of domain I^c, $I^c_{(0)}$, is needed. An easy way of predicting the $I^c_{(0)}$ is by finding the points (x_i, y_j), which is above the rigid flat.

Several numerical methods have been developed in the past 40 years in order to solve Eq. 4.7, namely, *matrix inversion* [32, 41] *Gauss-Seidel relaxation* [40], *Newton-Raphson relaxation* [40] and *variational method* [49, 50].

Matrix Inversion

The summation term in Eq. 4.7 can be treated as multiplication between the matrix $\mathbf{A}$ and unknown pressure vector $\mathbf{p}$:

$$\mathbf{p} = \mathbf{A}^{-1}(\mathbf{h} - d)$$

Matrix $\mathbf{A}$ is the influence coefficients assembly from the K_{ijkl}. Pressure vector, $\mathbf{p}$, can be solved by inverting $\mathbf{A}$. The disadvantage of the matrix inversion method is (1) unrealistic memory spaces are needed to save matrix $\mathbf{A}$, and (2) solving unknown pressure vector $\mathbf{p}$ by the direct solver, such as *Gaussian elimination*, requires $O(N^3)$ operations because $\mathbf{A}$ is dense and non-symmetric (here, N is the number of contacting points). Consequently, matrix inversion can only be used in the small-scale contact problem with less than thousands of points, even though it is robust. Matrix Inversion was a popular solver of rough surfaces contact model during the 1980s [41, 42, 43, 44].

Gauss-Seidel Relaxation

During one iteration, say i^{th} iteration, contact domain $I^c_{(i)}$ is fixed and Eq. 4.7 is a linear equation which can be solved by Gauss-Seidel relaxation

$$\bar{p}_{ij} = \tilde{p}_{ij} + w_1 \delta_{ij} \tag{4.8}$$

where

$$\delta_{ij} = h_{ij} - d - \sum_{m=0}^{n_x-1} \sum_{s=0}^{n_y-1} D_{ms}\, \tilde{p}_{kl}$$

where $\bar{p}_{ij}$ and $\tilde{p}_{ij}$ are the pressure value after and before the Gauss-Seidel relaxation at point (x_i, y_j). D_{11} is the influence coefficient when (i, j) coincides with (k, l). w_1 is the *under-relaxation coefficient* used to stabilize and in some cases accelerate the iteration process. However, Eq. 4.8, is not stable because changing the value of pressure at (x_i, y_j) may change the deformation of all the points within the domain I^c more or less [40]. Venner and Lubrecht [40] suggested to use the following correction scheme:

$$\bar{p}_{ij} = \tilde{p}_{ij} + \delta_{ij} - \frac{1}{4}(\delta_{i+1\ j} + \delta_{i-1\ j} + \delta_{i\ j+1} + \delta_{i\ j-1}) \tag{4.9}$$

where

$$\delta_{ij} = (h_{ij} - d - \sum_{m=0}^{n_x-1} \sum_{s=0}^{n_y-1} D_{ms}\, \tilde{p}_{kl})/(D_{11} - D_{12}/2 - D_{21}/2)$$

for 2 dimensional relaxation in order to stabilize the iteration scheme. The Gauss-Seidel relaxation scheme with Eq. 4.9 has been wildly used in both elastohydrodynamic lubrication [45, 40] and dry rough surface contact[46, 47, 48] problems.

Newton-Raphson Relaxation

Rewriting Eq. 4.5 here

$$g_{ij} = \sum_{(x_i,y_j)\in I^c} \sum_{(x_k,y_l)\in I^c} D_{ms}\, p_{kl} + d - h_{ij}$$

Expanding the above equation in Taylor series and only keeping the first direvative term, we have

$$g_{ij} + \frac{\partial g_{ij}}{\partial p_{kl}} \delta p_{kl} = 0, \quad (x_i, y_j), (x_k, y_l) \in I^c \tag{4.10}$$

where $\frac{\partial g_{ij}}{\partial p_{kl}} = D_{ms}$. As the distance between (x_i, y_j) and (x_k, y_l) increases, value of D_{ms} decreases dramatically. This implies that those pressure changes far away from point (i,j) may have little effect on the equilibrium of Eq. 4.5. Thus only 5 points: (x_i, y_j), (x_{i+1}, y_j), (x_{i-1}, y_j), (x_i, y_{j+1}), (x_i, y_{j-1}), are picked

$$D_{11} \delta p_{ij} + D_{21} \delta p_{i+1\ j} + D_{21} \delta p_{i-1\ j} + D_{12} \delta p_{i\ j+1} - D_{12} \delta p_{i\ j-1} = -g_{ij}$$

to join the correction scheme. Line relaxation can be used to perform more robust iteration:

$$D_{11} \delta \bar{p}_{ij} + D_{21} \delta \bar{p}_{i+1\ j} + D_{21} \delta \bar{p}_{i-1\ j} = -g_{ij} - D_{12} \delta \tilde{p}_{i\ j+1} - D_{12} \delta \bar{p}_{i\ j-1} \tag{4.11}$$

$\delta \bar{p}_{ij}$ and $\delta \tilde{p}_{i\ j}$ are the residual pressure at (x_i, y_j) after and before one complete Newton-Raphson line iteration. Eq. 4.11 is a non-linear equation and an extra iteration is needed to ensure the accuracy of $\delta \bar{p}_{ij}$ satisfies the required convergence criterion. An even simpler method can be achieved by only using 3 points along the same dominant direction, e.g.,

$$D_{11} \delta \bar{p}_{ij} + D_{21} \delta \bar{p}_{i+1\ j} + D_{21} \delta \bar{p}_{i-1\ j} = -g_{ij} \tag{4.12}$$

to avoid the nonlinearity. Pressure solution p is then updated by Eq. 4.8.

Variational Method

Kalker and van Randen [49] established the variational principle for the frictionless contact problem and applied it to frictionless non-Hertzian contact problems. The unique pressure solution causes the total complementary energy to take the minimum value. However, variational method cannot guarantee the solution satisfying exactly the boundary condition

in Eq. 4.6 [50]. Application of the variational method can be found in rough surface contact [50] and rough contact with coated layer [51].

4.4 Fast algorithm for deformation integral

Let us rewrite the deformation integral, Eq. 4.4, in the governing equation Eq. 4.5

$$w_{ij} = \sum_{m=0}^{n_x-1} \sum_{s=0}^{n_y-1} D_{ms}\, p_{kl}, \quad (x_i, y_j), (x_k, y_l) \in \Omega.$$

If iterative methods, e.g., Gauss-Seidel, Netwon-Raphson and variational methods, are used in solving Eq. 4.5, then the above integral equation needs to be evaluated in each iteration (see Eq. 4.8 and 4.12). For the current 3D rough surface contact, $O(N^2)$ operations are required to compute the whole surface deformation. As more and more sampling points are used in modeling the rough surface, computational time for each iteration increases dramatically to an unrealistic value. Currently, the maximum number of sampling points used in rough surface contact modeling with the application of BEM is 16385×16385 [48]. In order to speed up the evaluation of surface displacement, two fast algorithms, namely *Multi level multi integration (MLMI)* and *fast Fourier transformation (FFT)*, are developed and wildly used in tribology.

Multi Level Multi Integration (MLMI)

Multi level multi integration (MLMI) method was developed by Brandt and Lubrecht [52] based on the idea of the multi-grid method which was originally used in solving elasto-hydrodynamic lubrication problem. Evaluation of w_{ij} is done on the coarsest level with the minimum number of points. Pressure distribution p_{ij} on the finest grid is transformed to the coarsest level by a restriction technique. After the evaluation of w_{ij} on the coarsest level, w_{ij} is transformed back to finest grid by a prolongation technique. By the help of MLMI, only $O(NlogN)$ operations are required to solve the deformation integral. The application of the MLMI method can be found in the area of elastohydrodynamic lubrication [45, 40]

and contact mechanics [46, 53, 57, 47, 48].

Fast Fourier Integration

The fast Fourier transformation method was first introduced by Stanley and Kato [50] for solving deformation of rough surface contact. Johnson et al. [31], however, may be the first to apply the Fourier transformation in waviness contact. In the Westergarrd solution of sinusoidal surfaces contact [30], we can find the correlation between the pressure p and surface displacement u when complete contact occurs:

$$p(x, y) = \cos(\alpha \mathrm{x})\cos(\beta \mathrm{y})$$
$$w(x, y) = \frac{2}{E'\left(\alpha^2 + \beta^2\right)^{1/2}}\cos(\alpha \mathrm{x})\cos(\beta \mathrm{y})$$
$$\alpha = \frac{2\pi n}{L_x}, \quad \beta = \frac{2\pi m}{L_y}.$$

A similar conclusion can also be found in sinusoidal profile (2D) contact. By decomposing the known pressure distribution p into the frequency domain by FFT [58], we can obtain the corresponding amplitudes of surface displacement. Then surface displacement w_{mn} corresponding to the certain frequency pair (m, n) can be found by an inverse FFT. Then the resultant surface displacement w can be evaluated by the superposition of w_{mn}. Again, $O(N^2)$ operations are reduced to $O(NlogN)$. The *FFT-based method developed by Stanley and Kato, however, is strictly applicable to the periodic discrete domain only.* Consequently, this makes the FFT-based method ideal for solving contact problems for nominally flat rough surfaces which can be modeled periodically, see Fig. 3.5. Rough surfaces in concentrated contact problems, i.e., finite nominal contact areas, are non-periodic and application of this FFT-based method in such cases may introduce error [53, 55].

To address this issue, Nogi and Kato [54] developed a different FFT-based method. Their ideal is to transfer the deformation integral: $\mathbf{w} = \mathbf{D}\,\mathbf{p}$ to frequency domain. By multiplying the Fourier transforms of $\mathbf{D}$ and $\mathbf{p}$, we can obtain the value of w_{ij} through

inverse Fourier transformation

$$\mathbf{w} = \text{ifft2}(\text{fft2}(\mathbf{D})\ \text{fft2}(\mathbf{p}))$$

where ifft2() and fft2() are 2 dimensional inverse FFT and FFT, respectively. Different from the FFT-based method developed by Stanley and Kato, this method is only valid for non-periodic domain, i.e., valid for concentrated contact problems only.

However, the FFT-based method developed by Nogi and Kato may bring errors at boundary of nominal area [55]. Liu et al. [55] developed a FFT-based method (DC-FFT method) and can help to avoid the errors at the borders of the domain.

4.5   Convergence criterion and surface separation

Different numerical methods, e.g., matrix inversion, Gauss-Seidel, Newton-Raphson and variational methods, are discussed in details in Section. 4.3. As the ith iteration is finished, convergence of the predicted pressure $\bar{p}_{(i)}$, is checked by

$$||\bar{p}_{(i)} - \bar{p}_{(i-1)}||_2/||\bar{p}_{(i)}||_2 < \delta_p \tag{4.13}$$

where $||(\bullet)||_2$ is the 2-norm. In order to make sure that contact area, A, converges and has similar accuracy, the contact area solution after each iteration is also checked via

$$||\bar{A}_{(i)} - \bar{A}_{(i)}||_2/||\bar{A}_{(i)}||_2 < \delta_a \tag{4.14}$$

where $\delta_a = 1/(n_x\ n_y)$. The iteration process will be terminated until the above two criterions, Eq. 4.13 and Eq. 4.14, is satisfied simultaneously.

As the total contact load, P, increases, the deformation of the surfaces becomes more severe and this may bring numerical difficulties to the iterative method. In order to gain a convergence solution, the *under-relaxation coefficient*, w_1, in Eq. 4.8 needs to be adaptively

adjusted by $w_1 = w_1/a$, 1.2 is selected as the value of a in this study, if solution is found to be divergent. 0.1 is chosen as the initial value of w_1. Also, in order to increase the convergent rate, the load step is divided into N substeps and the converged pressure solution $p_{(i)}$ obtained at substep i is used as the initial pressure guess at substep $i + 1$.

According to the assumption of a semi-infinite body, if the surface separation d is measured from the mean level of the undeformed rough surface, the surface separation may finally reach negative infinity as contact load increases. It is possible, however, to defined a new surface separation, d', measured from the mean level of deformed rough surface

$$d' = d - (\sum_{i=1}^{n_x} \sum_{j=1}^{n_y} w_{ij})/(n_x n_y) \tag{4.15}$$

which excludes the rigid body displacement of the mean level. w_{ij} is the displacement on $z = 0$ plane along the z direction at (x_i, y_j). Evidently, d' varies from an initial value of d at first contact to 0 when complete contact is reached. A similar approach is considered by Wilson et al. [56]

4.6 Results and discussion

In this study, the governing Eq. 4.7 is solved by two different methods. One uses the Newton-Raphson iterative method and the FFT-based fast integral method by Liu et al. [54] (NR+DC-FFT). Another one uses the variational method and the FFT-based fast integral method by Stanley and Kato [50] (VM+FFTSK). The same dimensionless group are used for the results in order to compare with the FE model: $P^* = P/(A_n E^*)$, $A^* = A/A_n$.

Fig. 4.3 shows a good agreement of the contact load to area relation of surface 1 predicted by the VM+FFTSK and the FE model. The FE Model is proved earlier that it is suitable for modeling the nominally flat rough surface contact with periodic domain. NR+DC-FFT overestimates the contact load for a given contact area and the difference increases as contact area increases. A possible reason causing the solution of NR+DC-FFT

to be different from that of VM+FFTSK and the FE model can be found in Fig. 4.5. When the DC-FFT is selected as the fast integral method, the contact problem is defined as shown in Fig. 4.5(a). As shown, a finite rigid flat is contacting a semi-infinite body with a rough surface. When the load P is applied on the rigid flat, deformation of rough surface is dominant comparing to that of the domain out side the rough surface contact region, see Fig. 4.5(c). Tension on the top surface of the semi-infinite body can be found and this may cause more material to slip from the borders of the contact region in stead of occupying the gap between the rough surface and the rigid flat. This tension force may dramatically cause a drop of contact area. When the FFTSK is solved using the fast integral method, rough surface contact pairs distributes periodically (cyclically), as shown in Fig. 4.5(b). As the load P is applied on the rigid flat, the top surface of the semi-infinite body deforms uniformly, see Fig. 4.5(d). According to mass conservation, surface points within the contact region have no where to flow except to occupy the gap between the rough surface and the rigid flat. In Fig. 4.5(c), the tangential displacement of surface points is considerable due to surface tension. Those tangential displacements may delay the formation of a larger contact area. That is why the contact area A^* predicted by NR+DC-FFT is underestimated for a given contact load P^*. However, the gap can be found between the solutions of surface 2 predicted by VM+FFTSK and the FE model (Fig. 4.4). Difference may be caused by anisotropic nature of surface data.

4.7   Conclusion

In this chapter, application of the boundary element method is discussed in details. The contact load to area relations obtained from the BEM and the FEM are in good agreement if the same boundary conditions are chosen. For elastic rough surface contact, the boundary element method has a great advantage in saving computation time. The rough surface meshing process in the commercial FEM software, e.g., ANSYS$^{\text{TM}}$, is tedious and a large number of sampling points ($> 400 \times 400$) is not allowed due to unrealistic computation time

Figure 4.3: Contact area to load relation of surface 1 predicted by the boundary element method and the finite element method.

and lack of storage capacity. The FEM, however, may have advantage when deformation between rough surfaces is nonlinear, e.g., elastic-plastic, viscous-elastic and creep.
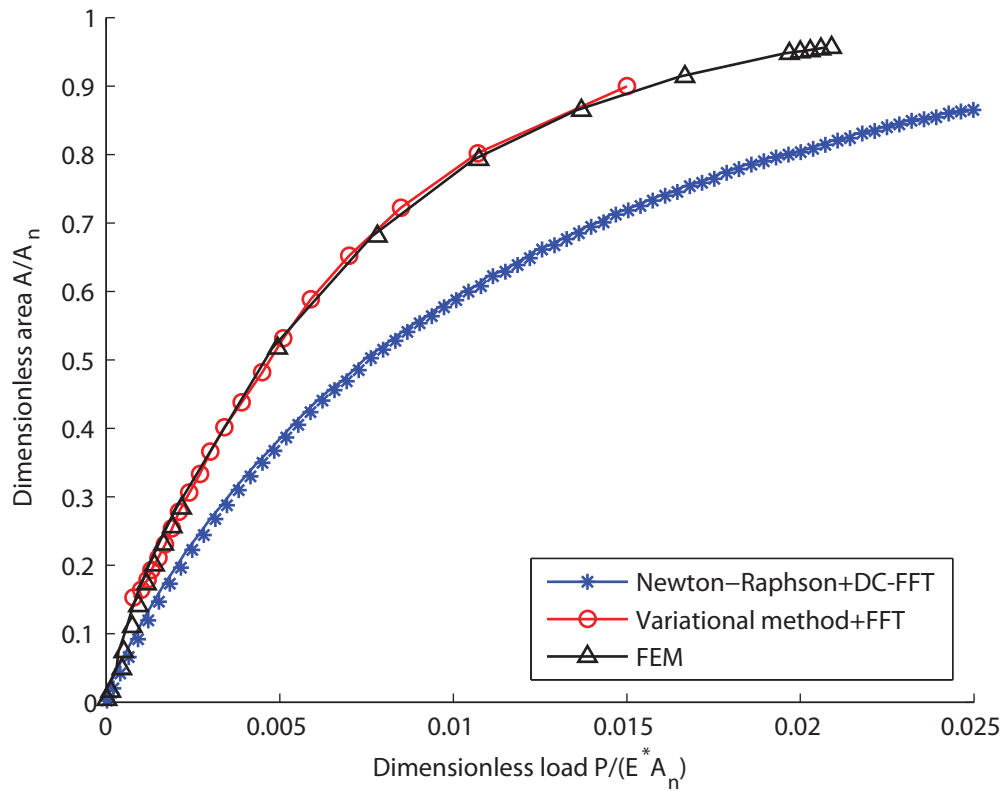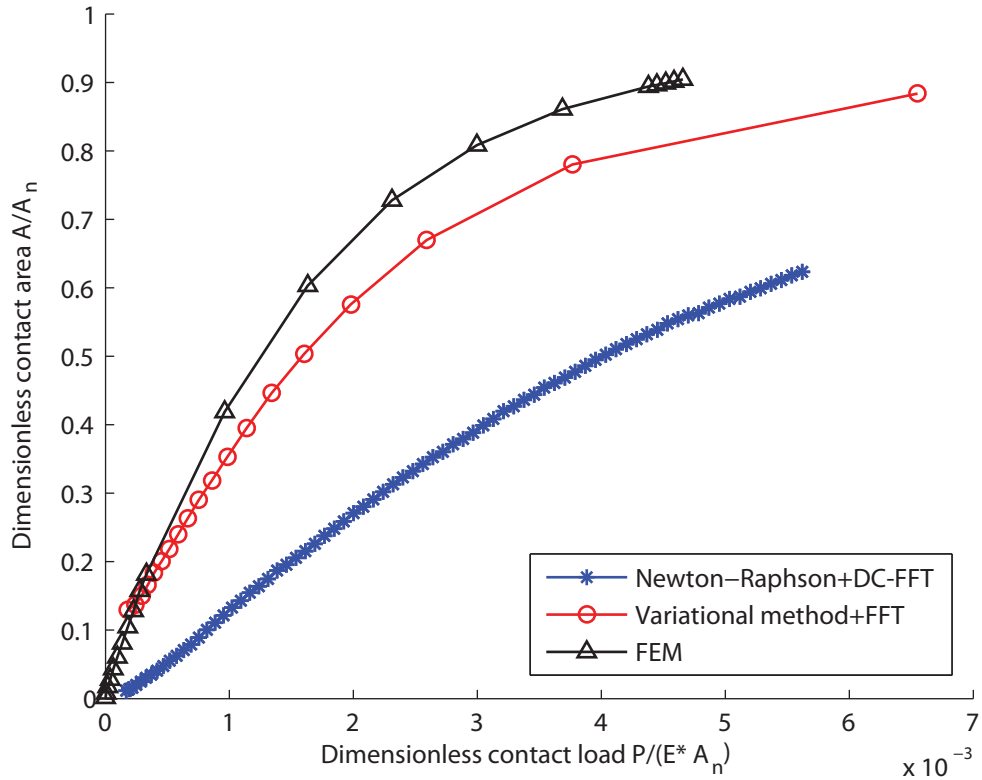
Figure 4.4: Contact area to load relation of surface 2 predicted by the boundary element method and the finite element method.
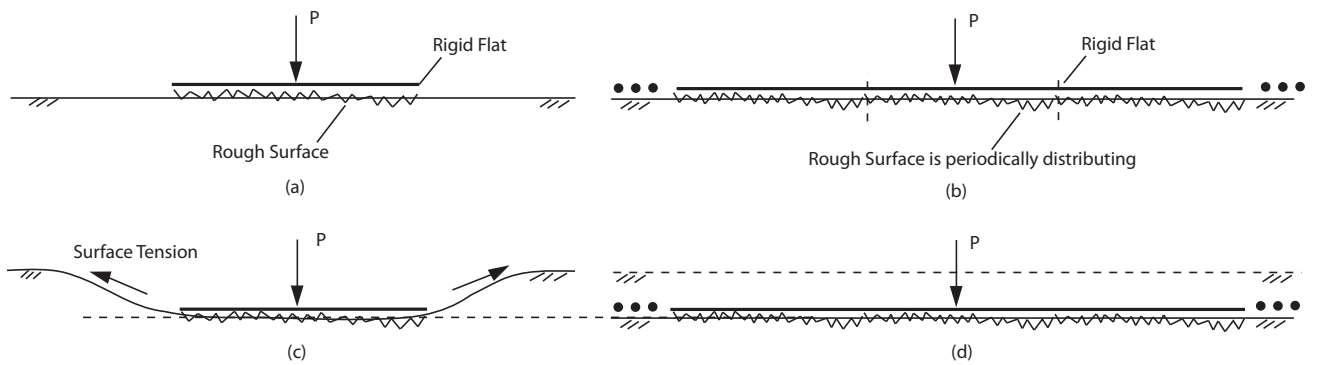

Figure 4.5: Schematic representation of rough surfaces deformation corresponding to different FFT-based fast integral method: NR+DC-FFT before (a) and after (c) deformation; VM+FFTSK before (b) and after (d) deformation.

Chapter 5

Conclusion and future work

In the current thesis, developments and applications of statistical, multi-scale, semi-numerical and deterministic numerical models are discussed. According to the conclusions of each chapter, we can conclude that the BEM has the advantages in modeling the rough surface contact among all the numerical models.

In the future work, current rough surface contact model built by the BEM will include the effect of friction for both full stick and partial slip conditions. Additionally, elastoplastic and adhesion can also be easily embedded in the framework of BEM.

The two asymptotic solutions with $min(B_{max})$ and $max(B_{max})$ in the conclusion of Chapter 2 can be used to curve-fit the empirical solution of elastic rough contact for isotropic surface. For anisotropic surface, the accurate model of anisotropic sinusoidal contact should be derived.

Bibliography

[1] Goryacheva, I.G., 1998 "Contact Mechanics in Tribology," Kluwer, pp.11-12

[2] Thomas, T.R., 1982 "Rough Surfaces," Longman, pp.92

[3] Greenwood, J.A., and Williamson, J.B.P., 1966, "Contact of Nominally Flat Surfaces," Proc. R. Soc. London, Ser. A, **295**, pp. 300-319.

[4] Chang, W.R., Etsion, I., and Bogy, D.B., 1987, "Elastic Plastic Model for the Contact of Rough Surfaces," ASME J. Tribol., **109**, pp. 257-262.

[5] Jackson, R.L., and Green, I., 2005, "A Finite Eleemnt Study of Elasto-Plastic Hemispherical Contact Against a Rigid Flat," ASME J. Tribol., **127**, pp. 343-354.

[6] Brizmer, V., Kligerman, Y., and Etsion, I., 2006, "The Effect of Contact Conditions and Material Properties on the Elasticity Terminus of a Spherical Contact," J. Mech. Mater. Struc., **1**, pp. 865-879.

[7] Zhao, Y., Maletta, D.M., and Chang, L., 2000, "An Asperity Microcontact Model Incorporating the Transition From Elastic Deformation to Fully Plastic Flow," ASME J. Tribol., **122**, pp. 86-93.

[8] Kogut, L., and Etsion, I., 2002, "Elastic-Plastic Contact Analysis of a Sphere and a Rigid Flat," ASME J. Appl. Mech., **69**(5), pp. 657-662

[9] Whitehouse, D.J., and Archard, J.F., 1970, "The Properties of Random Surfaces of Significance in Their Contact," Proc. Roy. Soc. Lond A., **316**, pp. 97-121.

[10] Onions, R.A., and Archard, J.F., 1973, "The Contact of Surfaces Having a Random Structure," J. Phys. D: Appl. Phys., **6**, pp. 289-304.

[11] Nayak, P.R., 1971, "Random Process Model of Rough Surfaces," AMSE J. Lub. Tech., **93**, pp. 398-407.

[12] Bush, A.W., Gibson, R.D., and Thomas, T.R., 1975, "The Elastic Contact of a Rough Surface," Wear, **19**, pp. 163-168.

[13] McCool, J.I., 1987, "Relating Profile Instrument Measurements to the Functional Performace of Rough Surfaces," ASME, J. Tribol., **109**, pp. 264-270.

[14] Carbone, G., and Bottiglione, F., 2008, "Asperity Contact Theories: Do They Predict Linearity Between Contact Area and Load?," J. Mech. Phys.Solids **56**, pp. 2555C2572.

[15] Zhao, Y., and Chang, L., 2001, "A Model of Asperity Interactions in Elastic-Plastic contact of Rough Surfaces," ASEM, J. Tribol., **123**, pp. 857-864.

[16] Ciavarella, M., Greenwood, J.A., and Paggi, M., 2008, "Inclusion of "Interaction" in the Greenwood and Williamson Contact Theory," Wear, **265**, pp. 729-734.

[17] Nayak, P.R., 1973, "Random Process Model of Rough Surfaces in Plastic Contact," Wear, **26**, pp. 305-333.

[18] Greenwood, J.A., 2007, "A Note on Nayak's Third Paper," Wear, **262**, pp. 225-227.

[19] Ma, X., Mahtijn, R., and Dik, S., 2010, "A Load Dependent Friction Model for Fully Plastic Contact Conditions," Wear, **269**, pp. 790-796.

[20] Sepehri, A., and Farhang, K., 2008, "On Elastic Interaction of Nominally Flat Rough Surfaces," ASME J. Tribol., **130**, pp. 011014-1

[21] Archard, J.F., 1957, "Elastic Deformation and the Laws of Friction," Proc. Roy. Soc. A., **243**, pp. 190-205.

[22] Mandelbrot, B.B., 1982, The Fractal Geometry of Nature, W.H.Freeman, New York.

[23] Majumdar, A., and Bhushan, B., 1991, "Fractal Model of Elastic-Plastic Contact Between Rough Surface," ASME J. Tribol., **113**, pp. 1-11.

[24] Ausloos, M., and Berman, D.H., 1985, A multivariate Weierstrass-Mandelbrot function, Proc. Roy. Soc. A., **400**, pp. 331-350.

[25] Yan, W., and Komvopoulos, K., 1998, Contact Analysis of Elastic-Plastic Fractal Surfaces., J. Appl. Phys., **84**(7), pp. 3617-3624.

[26] Kogut, L., and Jackson, R.L., 2006, "A Comparison of Contact Modeling Utilizing Statistical and Fractal Approaches," ASME J. Tribol., **128**, pp. 213-217.

[27] Majumdar, A., and Tien, C.L., 1990, "Fractal Characterization and Simulation of Rough Surfaces," Wear, **136**, pp. 313-327.

[28] Voss, R.F., 1985, "Fractals in nature: from characterization to simulation," Springer-Verlag, Berlin, pp. 805.

[29] Jackson, R.L., and Streator, J.L., 2006, "A Multi-Scale Model for Contact Between Rough Surfaces," Wear, **261**, pp. 1337-1347.

[30] Westergaard, H.M., 1933, Bearing Pressures and Cracks, ASME J. Appl. Mech., **6**, pp. 49-53.

[31] Johnson, K.L., Greenwood, J.A., and Higginson, J.G., The Contact of Elastic Regular Wavy Surfaces, Int. J. Mech. Sci., **27**(6), pp. 383-396.

[32] Johnson, K.L., 1985, Contact Mechanics, Cambridge Univeristy Press.

[33] Krithivasan, V., and Jackson, R. L., 2007 "An Analysis of Three-Dimensional Elasto-Plastic Sinusoidal Contact," Tribol Lett, **27**(1), pp. 31-43.

[34] Jackson, R.L., and Green, I., 2011, "On the Modeling of Elastic Contact between Rough Surfaces," Tribol Trans, **54**, pp. 300-314.

[35] Jackson, R.L., 2010, "An Analytical Solution to an Archard-Type Fractal Rough Surface Contact Model," Tribol Trans, **53**(4), pp. 543-553.

[36] Thomson, M.K., 2010, "Considerations for the Incorporation of Measured Surface in Finite Element Models," SCANNING, **32**, pp. 183-198.

[37] Becker, A.A., 1992, The Boundary Element Method in Engineering, McGrall-Hill, London.

[38] Liu, Y.J., 2009, Fast Multipole Boundary Element Method - Theory and Applications in Engineering, Cambridge University Press, Cambridge.

[39] Love, A.E.H., 1952, A Treatise on the Mathematical Theory of Elasticity, 4th Edn, Cambridge University Press, Cambridge.

[40] Venner, C.H., 2000, Multilevel Methods in Lubrication, Elsevier, Amsterdam.

[41] Webster, M.N., and Sayles, R.S., 1986, A Numerical Model for the Elastic Frictionless Contact of Real Rough Surfaces, ASME J. Tribol, **108**, pp. 314-320

[42] Lei, W.T. and Cheng, H.S., 1985, Computer Simulation of Elatic Rough Surface Contacts, Trans. ASLE, 1985, **28**, pp. 172-180.

[43] Seabra, J., and Berthe, D., 1987, Influence of Surface Rougness and Waviness on the Normal Pressure Distribution in the Hertzian Contact, ASME J. Tribol, **109**, pp. 462-470.

[44] West, M.A., Webster, M.N., and Sayles, R.S., 1987, A New Method for Rough Surface Contact Analysis, Proc. I. Mech. E., **C161/87**, pp.945-955.

[45] Venner, C.H., 1991, Multigrid solution to the EHL line multigrid techniques, Ph.d Thesis, University of Twente, Enschede.

[46] Lubrecht, A.A., and Ioannides, E., 1991, "Problem and the Associated Subsurface Stress Field, Using Multilevel Techniques," J. Tribol, **113**, pp. 128-133.

[47] Colin, F., 2001, "Comparison of FFT-MLMI for Elastic Deformation Calculations," J. Tribol, **123**, pp. 884-887.

[48] Sainsot, P., and Lubrecht, A.A., 2010, "Efficient Solution of the Dry Contact of Rough Surfaces: A Comparison of Fast Fourier Transform and Multigrid Methods," Proc. IMechE Part J: J. Engineering Tribology., **225**, pp. 441- 448.

[49] Kalker, J.J., and van Randen, Y., 1972, "A Minimum Principle for Frictionless Elastic Contact with Application to Non-Herzian Half-Space Contact Problems," J. Eng. Math., **6**, pp. 193.

[50] Stanley, H.M., and Kato, T., 1997, "An FFT-Based Method for Rough Surface Contact," ASME J. Tribol, **119**, pp. 481-485.

[51] Bhushan, B., and Peng, W., 2001, "Contact Mechanics of Multiplayered Rough Surfaces," ASME Appl Mech Rev, **55**(5), pp. 435-480.

[52] Brandt, A., and Lubrecht, A.A., 1990, "Multilevel Matrix Multiplication and Fast solution of Integral Equations," J. Comp. Phys., **90**, pp. 348-370.

[53] Polonsky, I.A., and Keer, L.M., 1999, "A Numerical Method for Solving Rough Contact Problems Based on the Muti-Level Multi-Summation and Conjugate Gradient Techniques," Wear, **231**, pp. 206-219.

[54] Nogi, T., and Kato, T., 1997, Influence of A Hard Surface Layer on the Limit of Elastic Contact:Part I. Anlysis Using A Real Surface Model, ASME J. Tribol., **119**, pp. 493-500.

[55] Liu, S.B., Wang, Q., and Liu, G., 2000, "A Versatile Method of Discrete Convolution and FFT(DC-FFT) for Contact Analyses," Wear, **243**, pp. 101-111.

[56] Wilson, W.E., Angadi, S.V., and Jackson, R.L., 2010, "Surface Separation and Contact Resistance Considering Sinusoidal Elastic-Plastic Multi-Scale Rough Surface Contact," Wear, **268**, pp. 190-201.

[57] Polonsky, I.A., and Keer, L.M., 2000, "Fast Methods for Solving Rough Contact Problems: A Comparative Study," ASME J. Tribo., **122**, pp. 36-41.

[58] Cooly, C.W., and tukey, J.W., 1965, "An Algorithm for the Machine Calculation of Complex Fourier Series," Math. Comput., **19**, pp. 297-301.

[59] Komvopoulos, K., and Choi, D.H., 1992, "Elastic Finite Element Analysis of Multi-Asperity Contacts," ASME J. Tribo, **114**, pp. 823-831.

[60] Hyun, S., Pei, L., Molinari, J.F., and Robbins, M., 2004, "Finite Element Analysis of Contact Between Elastic Self-Affine Surfaces," Phy. Rev. E, **70**, 026117.

[61] Hyun, S., and Robbins, M., 2007, "Elastic Contact Between Rough Surface: Effect of Roughness at Large and Small Wavelengths," Tribology International, **40**, pp. 1413-1422.

[62] Pei, L., Hyun, S., Molinari, J.F., and Robbins, M., 2005, "Finite Element Modeling of Elasto-Plastic Contact Between Rough Surfaces," J. Mech. Phys. Solids, **53**, pp. 2385-2409.

[63] Sahoo, P., and Ghosh, N., 2007, "Finite Element Contact Analysis of Fractal Surfaces," J. Phys. D: Appl. Phys. **40**, pp. 4245-4252.

[64] Walter, C., and Mitterer, C., 2009, "3D versus 2D Finite Element Simulation of the Effect of Surface Roughness on Nanoindentation of Hard Coatings," Surface and Coatings Technology, **203**, pp. 3286-3290.

[65] Yastrebov, V.A., Durand, J., Proudhon, H., and Cailletaud, G., 2011, "Rough Surface Contact Analysis by Means of the Finite Element Method and of a New Reduced Model," C.R.Mecanique, **339**, pp. 473-490.

[66] Bryant, M.J., Evans, H.P., and Snidle, R.W., 2011, "Plastic Deformation in Rough Surface Line Contacts-A Finite Element Study," Tribology International, **46**(1), pp. 269-278.

[67] Olshevskiy, A., Yang, H.I., and Kim, C.W., 2011, "Finite Element Simulation of Inelastic Contact for Arbitrarily Shaped Rough Bodies," Proc. IMechE. Part C:J. Mechanical Engineering Science, **0**, pp. 1-12.

[68] Megalingam, A., and Mayuram, M.M., 2012, "Comparative Contact Analysis Study of Finite Element Method Based Deterministic, Simplified Multi-Asperity and Modified Statistical Contact Models," ASME J. Tribo, **134**, 014503.

[69] Thompson, M.K., 2007, A Multi-Scale Iterative Approach for Finite Element Modeling of Thermal Contact Resistance, Ph.D. Thesis, Massachusetts Institute of Technology.

[70] Temizer, I., 2010, "Thermomechanical Contact Homogenization with Random Rough Surfaces and Microscopic Contact Resistance," Tribology International, **44**, pp. 114-124.

[71] ANSYS Help V13.0, ANSYS Inc

[72] Jamari, J., de Rooij, M.B., and Schipper, D.J., 2007, "Plastic Deterministic Contact of Rough Surfaces," ASME J. Tribo, **129**, pp. 957- 962.

[73] Pasaribu, H.R., and Schipper, D.J., 2005, "Application of a Deterministic Contact Model to Analyze the Contact of a Rough Surface Against a Flat Layered Surface," ASME J. Tribo, **127**, pp. 451- 455.

[74] Hariri, A., Zu, J.W., and Ben Mrad, R., 2006, "n-Point Asperity Model for Contact Between Nominally Flat Surfaces," ASME J. Tribo, **128**, pp. 505-514.

[75] Ciaverella, M., Delfine, V., and Demelio, G., 2006, "A "re-vitalized" Greenwood and Williamson Model of Elastic Contact Between Fractal Surfaces," J. Mech. Phys. Solids, **54**, pp. 2569-2591.

[76] Yeo, C.D., Katta, R.R., Lee, J.K., and Polycarpou, A.A., 2010, "Effect of Asperity Interactions on the Rough Surface Elastic Contact Behavior: Hard Film on Soft Substrate," Tribology International, **43**, pp. 1438-1448.

[77] Afferrante, L, Carbone, G., and Demelio, G., 2012, "Interacting and Coalescing Hertzian Asperities: A New Multiasperity Contact Model," Wear, **278-279**, pp. 28-33.

[78] Nayak, P.R., 1973, "Random Process Model of Rough Surfaces in Plastic Contact," Wear, **26**, pp. 305-333.

[79] Eid, H., and Adams, G.G., 2007, "An Elastic-Plastic Finite Element Analysis of Interacting Asperities in Contact with a Rigid Flat," J. Phys. D: Appl. Phys., **38**, pp. 2841-2847.

[80] Greenwood, J.A., 2007, "A Note on Nayak's third paper," Wear, **262**, pp. 225-227.

[81] Ma, X., de Rooij, M.B., and Schipper, D.J., 2010, "A Load Dependent Friction Model for Fully Plastic Contact Conditions," Wear, **269**, pp. 790-796.

Appendix A

Influence Coefficient K_{ijkl}

Finding the stresses and displacements in an elastic half-space due to the point load belonging to the Boussinesq problem [32]. Love [39] derived the vertical displacement of an arbitrary surface point (x_i, y_j) due to the uniform pressure distribution $p = p_{kl}$ within the rectangular area $2a \times 2b$ with the center (x_k, y_l), see Fig. 2.1.1.

$$\frac{\pi E^* w_{ij}}{p} = K_{ijkl} = (x + a) \ln \left[\frac{(y + b) + \{(y + b)^2 + (x + a)^2\}^{1/2}}{(y - b) + \{(y - b)^2 + (x + a)^2\}^{1/2}} \right] \qquad (A.1)$$

$$(y + b) \ln \left[\frac{(x + a) + \{(y + b)^2 + (x + a)^2\}^{1/2}}{(x - a) + \{(y + b)^2 + (x - a)^2\}^{1/2}} \right]$$

$$(x - a) \ln \left[\frac{(y - b) + \{(y - b)^2 + (x - a)^2\}^{1/2}}{(y + b) + \{(y + b)^2 + (x - a)^2\}^{1/2}} \right]$$

$$(y - b) \ln \left[\frac{(x - a) + \{(y - b)^2 + (x - a)^2\}^{1/2}}{(x + a) + \{(y - b)^2 + (x + a)^2\}^{1/2}} \right]$$

where

$$x = |x_i - x_k|, \quad y = |y_j - y_l|$$